Alma Mater Studiorum - Università di Bologna

DOTTORATO DI RICERCA IN

IL FUTURO DELLA TERRA, CAMBIAMENTI CLIMATICI E SFIDE SOCIALI

Ciclo 35

Settore Concorsuale: 04/A4 - GEOFISICA

Settore Scientifico Disciplinare: GEO/10 - GEOFISICA DELLA TERRA SOLIDA

A TRANS DIMENSIONAL INVERSION ALGORITHM TO MODEL DEFORMATION SOURCES WITH UNCONSTRAINED SHAPE IN FINITE ELEMENT DOMAINS

Presentata da: Erica De Paolo

Coordinatore Dottorato

Silvana Di Sabatino

Supervisore

Elisa Trasatti

Co-supervisore

Maria Elina Belardinelli

Esame finale anno 2023

Table of Contents

Abstract 1

Introduction 2

Chapter 1: The elementary source unit in the FEM domain 11

1.1. The Finite Element domain 12

1.2. The elementary source unit 13

Chapter 2: Benchmarking of synthetic source assemblies 18

2.1. The spherical source. 19

2.2. The vertical spheroid. 21

2.3. The spheroid with dip and strike 23

2.4. The sill-like source. 26

Chapter 3: The trans-dimensional inversion algorithm 29

3.1. The Bayesian inference in inversion methods 30

3.2. The Reversible-Jump McMC 31

3.3. Voronoi cells 32

3.4. RJMcMC recipe 34

3.5. Algorithm workflow and performances 36

3.5.1. Model inputs: Data, Responses, Prior 37

3.5.2. The main loop: Candidate model and Metropolis' rule 39

3.5.3. Model outputs 42

3.5.4. Performances 43

Chapter 4: Algorithm validation through synthetic testing 46

4.1. From analytical to V-cells source representation 47

4.2. Data and fit 48

4.3. Sampling of the model space 49

4.4. Misfit and parsimonious solution 52

Chapter 5: The Long Valley caldera case study 55

5.1. Introduction 56

5.2. Data 57

5.2.1. InSAR 57

5.2.2. GNSS 59

5.3. Deformation source modeling 61

5.4. Results and discussions 63

5.5. Conclusions 66

Conclusions and future developments 68

References 72

Supplementary materials 80

Abstract

Ground deformation provide valuable insights on subsurface processes with pattens typically reflecting the characteristics of the source at depth. In active volcanic sites displacements can be observed in unrest phases; therefore, a correct interpretation is essential to assess the hazard potential. Inverse modeling techniques are employed to obtain quantitative estimates of parameters describing the source. However, despite the robustness of the available approaches, a realistic imaging of these reservoirs is still challenging. While analytical models return quick but simplistic results, assuming an isotropic and elastic crust, more sophisticated numerical models, accounting for the effects of topographic loads, crust inelasticity and structural discontinuities, require much higher computational effort and information about the crust rheology may be challenging to infer. All these approaches require a-priori source shape constraints, influencing the reliability of the solution. In this thesis, we present a new approach aimed at overcoming the aforementioned limitations. We model deformation sources free of a-priori shape constraints, benefiting from the advantages of FEM simulations, but with a cost-efficient procedure. The source is represented as an assembly of elementary units, consisting in cubic elements of a regular FE mesh loaded with a unitary stress tensors. The surface response due to each of the six stress tensor components for each unit is computed and linearly combined to obtain the total displacement of the composite source. In this way, the source can assume potentially any shape. Our direct tests prove the equivalence of the deformation fields due to our assembly, appropriately loaded, and that caused by corresponding cavities with uniform boundary pressure. Our ability to simulate pressurized cavities in a continuum domain permits to pre-compute unitary surface responses, avoiding remeshing. A Bayesian trans-dimensional inversion algorithm implementing this strategy is developed, using 3D Voronoi cells to sample the model domain, selecting the elementary units contributing to the source solution and those remaining inactive as part of the crust.

Introduction

A wide range of natural and anthropogenic phenomena, such as landslides, glaciers retreat, seismic and volcanic processes, can be investigated through the analysis of the ground displacement they cause (e.g., Biggs and Wright, 2020; Poland and de Zeeuw-van Dalfsen, 2021). In particular, subsurface processes can produce deformation signals as a response to the stress field variations in the Earth's crust, caused by mass redistributions and pressure changes. By means of geodetic measurements, we are able to retrieve valuable insights about processes that are not directly accessible, improving our capacity of understanding deep systems and, in the case of natural hazards, of better assessing the hazards.

Permanent, or campaign style, Global Navigation Satellite Systems (GNSS) geodetic monitoring networks, leveling benchmarks and borehole stations (tiltmeters and strain meters) are routinely supported by other satellite-based systems, such as those having Synthetic Aperture Radar (SAR) sensors onboard. The most widely used application of SAR imagery is the InSAR (Interferometric SAR), exploiting phase differences between successive radar acquisitions to detect ground changes over a chosen time period (e.g., days or months). Multi-temporal InSAR analysis of multiple images allows to depict ground velocities over longer timescales (months to years). InSAR data accuracy is in the order of 1 cm (Dzurisin, 2003) but the spatial resolution is very high, especially when compared to the discrete coverage of in-situ measurements (Casu et al. 2006).

In active volcanic areas, ground deformation can be observed in all the phases of activity (pre-, syn-, and post-eruptive), especially during the phases of unrest (Biggs et al., 2014 and references therein). The presence of an unrest period is typically determined by anomalous increase of seismicity, deformation, degassing and/or other signals (Acocella, 2019).

Not all the unrests lead to a volcanic eruption, as their nature can be linked to magma emplacement at shallow depths, as well as to hydrothermal activity or any far-field triggering events (Newhall and Dzurisin, 1988). In particular, uplift and subsidence, along with horizontal displacements, are commonly attributed to stress field variations in the crust caused by pressure and volume changes in deep reservoirs (e.g. due to magma injections) and/or by the ascent and emplacement of a shallow magma intrusions (i.e. dike) (Lisowski et al., 2007). Thus, our ability to predict periods with increased hazard potential relies, in part, on the correct interpretations of such signals (Rosi et al., 2022).

The interpretation of geodetic data in volcano monitoring typically aims at the retrieval of information about the deformation source at depth. In fact, the deformation field patterns we observe on the surface are highly dependent on the characteristics of the source. A link between observed deformation and the deep magmatic system, that we cannot not directly access, is provided by mathematical models. In particular, inverse modeling methods are employed to obtain quantitative estimates of parameters describing the deformation source such as: the location and the depth, the volume and pressure changes and the shape. The goodness of these models is often evaluated in terms of fit, with a comparison between the observed system response and that predicted by a theoretical forward model. In principle, considering equal data quality, the more sophisticated is the forward model, the closer we expect to be to a realistic representation of the source. However, sophistication typically involves higher computational cost, encouraging the use of simpler models and a-priori assumptions. Therefore, a wide variety of modeling methods is currently available and in use, accounting for different orders of complexity and based on several types of statistical methods.

The simplest models assume the Earth's crust as an isotropic, elastic flat half-space, embedding inflating or deflating magma chambers with simple a-priori shape.

Despite these simplistic assumptions, these models are commonly employed for quick first-order estimations and short-term interpretation (Lisowski et al., 2007). The first application of an analytical volcanic source model Kilauea volcano (Mogi, 1958), the source is represented as a dimensionless centre of dilatation (i.e., point source). Since then, several other types of geometric source solutions have been proposed as, for example, spherical, spheroidal, sill-like and tabular (e.g. faults or dike intrusions) models, respectively described in McTigue (1987), Yang et al. (1988), Fialko et al. (2001) and Okada (1985). In addition, a more versatile point-source (i.e. moment tensor source) simulating several symmetric geometries by means of appropriate compositions of dipoles and double couples of forces, has been proposed by Davis (1986) and will be further described in this thesis, as one of the starting points from which we develop our original methodology. All these models (Figure 1) are implemented in open source modeling inversion tools such as dMODELS, GBIS and VSM, respectively presented by Battaglia et al. (2013), Bagnardi and Hooper (2018) and Trasatti (2022).

More complexities can be considered with Finite Element Methods (FEMs), in which the crust can be characterized with informations from geological (e.g., structural maps) and geophysical studies (e.g. seismic tomography models) of the study area, when available. In this way, a better representation of the natural medium (i.e. the crust) embedding the volcanic magma chamber, or in general the deformation source, can be modeled. The influence of crustal heterogeneities, such as the presence of rock formations with different rheological behavior and structural discontinuities, as well as the topography, has been proved to be relevant by several authors (Trasatti et al., 2003; Hickey et al., 2015). In fact, the stress field in the crust and, consequently, the deformation field on the surface can differ a lot when accounting for different complexities in a Finite Element Method model.

Although FEM-based numerical models provide more sophisticated solutions, they are not optimally suitable for the implementation in inversion frameworks, since each change in the position or dimension of the source would require computationally expensive re-meshing procedures.

For such reason, FEMs methods commonly rely on sources with fixed position and simplified geometries, such as those analytical presented above. Several geological and geophysical evidences demonstrate that magma chambers should be characterized by much more complex geometries (e.g. Smith et al., 2009; Burchardt et al., 2010; Huang et al., 2015), claiming the need for new modeling procedures.

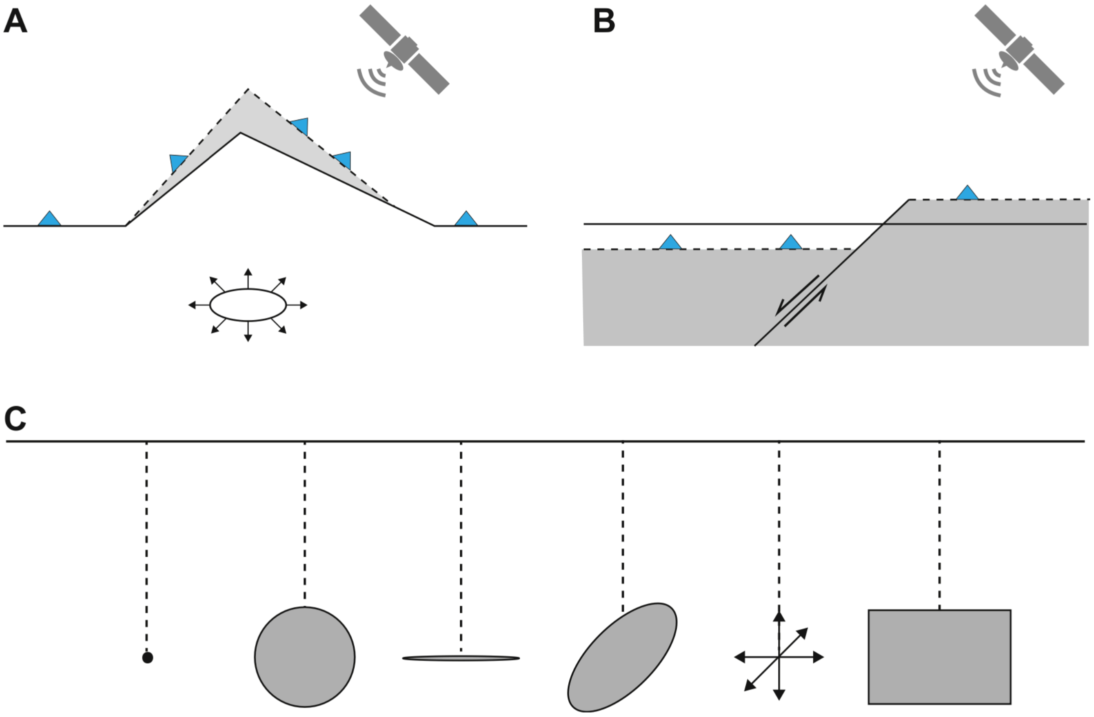

Figure 1. Geodetic measurements and deformation sources in inverse problems. a,b) Simplified sketch illustrating how over-pressures at depth and related stress field variations in the crust (a) or seismic fault slip (b) can cause measurable surface displacements. c) The most common analytical solutions for deformation sources, from left to right, isotropic point-source (Mogi, 1958), finite spherical source (McTigue, 1987), penny-shaped crack (Fialko et al., 2001), moment tensor source (Davis, 1986) and rectangular dislocation (Okada, 1985). Figure from Trasatti (2022).

In the past years, some authors attempted to develop geometry-free modeling schemes based on clusters of point pressure sources, i.e., Mogi (1958) source, in elastic half-space conditions (Mossop and Segall, 1999; Vasco et al., 2002; Masterlark and Lu, 2004; Camacho et al., 2011) or in FEM domains (Ronchin et al., 2017). In the first cases, the use of multiple isotropic point sources fails in representing a cavity of the same shape with constant overpressure on its boundary. This setting does not fulfill basic principles of continuum mechanics, since the sum of the surface displacements due by the single small cavities is different from those given by a cavity of the same shape (it holds only if the aggregation represents a sphere). In fact, according to Yang et al. (1988), the deformation field produced by a cavity with uniform pressure applied at the boundaries can be reproduced only by a distribution of appropriate dipoles and couples of forces mechanisms, with magnitudes ratios mimicking the mutual relationships existing among the source axis ratios (Figure 2).

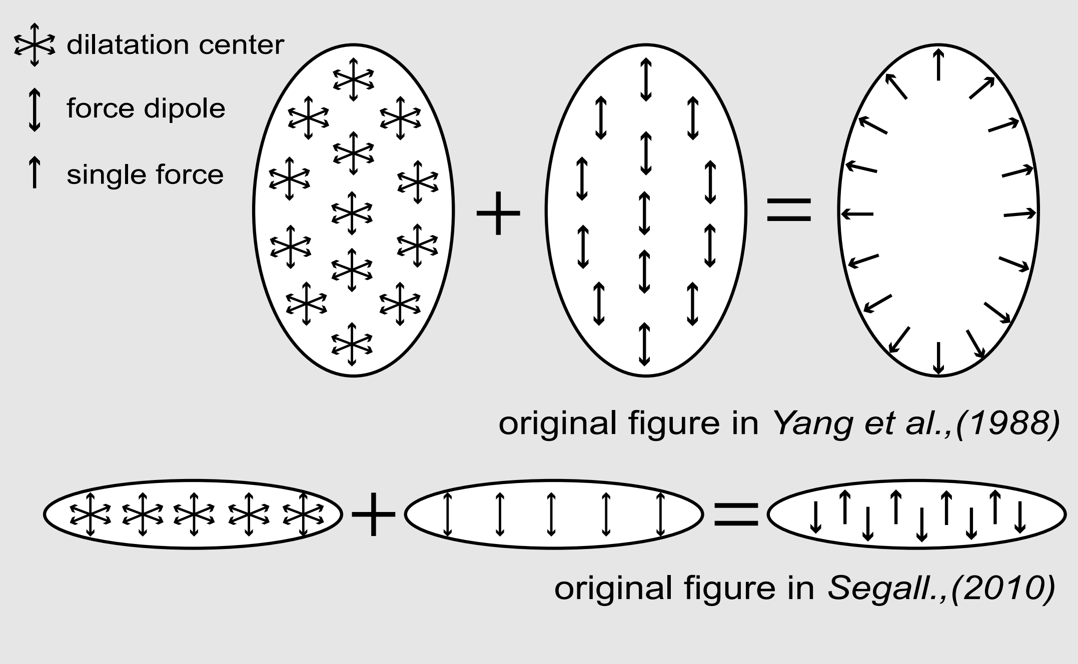

Figure 2. Uniform distributions of forces to reproduce a pressurized cavity. A uniform distribution of centers of dilatations and dipoles of forces reproduces an ellipsoidal cavity, according to Yang et al. (1988) and Segall (2010).

In addition, these methods based on analytical solutions are limited to the homogeneous elastic half-space, oversimplifying the solution of a source in a complex domain. Contrarily, the second type of approach, presented by Ronchin et al. (2017), has the advantage of using a Finite Element three-dimensional space, but it relies on another type of a-priori source shape constraint, as the FEM volume in which the source exists is derived from other independent data (e.g. seismic tomography). In this pre-defined portion of the model domain, pressurized points are distributed in the location of FE cubic element centers. These elements are removed iteratively from the meshed domain to form the pressurized cavity, representing the volcanic source. These pressure centers are characterized by non-uniform magnitudes estimated during the inversion. With this approach, the principle of uniform pressure at the source boundaries is, again, not fulfilled. Moreover, the process of removing one element at the time from the domain, together with the estimation of different magnitudes of pressure change in every location, makes this non-linear problem particularly expensive in terms of computation.

A strategy to model point-sources without a priori fixed shapes in Finite Element domains, avoiding re-meshing, is proposed by Trasatti et al. (2008). Based on Eshelby (1957) and Davis (1986), this strategy consists in the application of a stress tensor to the faces of a solid cubic element of the FEM, as a combination of dipoles and couples of forces, representing the six normal and shear components: σ_{xx}, σ_{yy}, σ_{zz}, σ_{xy}, σ_{yz}, σ_{zx}. In this way, a source that mimics the moment tensor solution described by Davis (1986) is implemented in a Finite-Element domain without cavities. The authors remark the advantages of this source representation, as the possible combinations of the potencies of the stress components foresee a subset of triaxial source shapes (Trasatti et al. 2008, 2011; Ferrari et al., 2015).

The moment tensor solution is interpreted by means of a diagonalization to find the principal moment values (i.e. the matrix eigenvalues). If these values are identical, the solution refers to an isotropic spherical source; otherwise, the solutions can range from a shear dislocation (a double couple) to ellipsoidal cavities with any orientation. The principal values ratios, in fact, are linked to the source axis ratios, as reported in Table 1 of Davis (1986), permitting to infer the source shape. However, this approach is only valid for a single element source in the point-source approximation, which means in the case of sources with dimensions significantly smaller than their depth (Segall, 2010). We know, nevertheless, that this is not always occurring in reality, particularly nowadays, thanks to the knowledge provided by high resolution geodetic data.

In this thesis, we present a new theoretical approach based on FEM to model deformation sources free of shape constraints, and the inversion algorithm implementing the methodology. This work aims at overcoming the aforementioned limitations, for a full exploitation of large amounts of geodetic data and for a more realistic representation of volcanic environments in inversion frameworks. We start from the approach of Trasatti et al. (2008), and we extend it to model a finite source made of several elementary units, represented as a cubic element loaded with the stress tensor. We reproduce the concept illustrated in Yang et al. (1988) and Segall (2010) (Figure 2), obtaining a uniform distribution of combinations of forces loading the elementary units with an appropriate stress tensor. We are able, then, to compute surface responses from a solid aggregate that numerically equals that of a cavity with uniform pressure at the boundary.

In conclusion, our method is (a) rigorous in terms of continuum mechanics; (b) allows for domain complexities; (c) is exempt from re-meshing iterations, as we use a full fixed mesh; (d) cost-efficient, thanks to pre-computed unitary surface responses scaled with only six factors, one for each stress component; and to a specifically designed Bayesian trans-dimensional inversion algorithm and represents a step forward in the state of the art in this field.

In the following chapters, a detailed description of the method is provided, starting from the initial conceptualization, including the design of the elementary unit in a FEM mesh and the initial synthetic testing phase, to the original inversion algorithm that has been developed to support our novel approach and the relative testing. Finally, we discuss the results and the future steps in the development of this approach, meant for being released as an open source software.

Chapter 1

The elementary source unit in the FEM domain

The objective of the thesis is, among all, to develop an original modeling approach for deformation sources free of shape constraints. To achieve this goal, we represent the source as a composite assembly of elementary units, fulfilling the continuum mechanics principles. The use of a FEM domain, together with the advantages of potentially account for complexities of the medium (e.g., heterogeneous crust layering, topography and discontinuities), allow us to build such source, thanks to its intrinsic property of being discretized. A variety of elementary unit configurations have been formulated and intensely tested in the preliminary phase of this study. We recognize that the most convenient strategy is to extend the Trasatti et al. (2008) approach to multiple contiguous FE elements. In this way, no modifications in the original mesh are required, as the final modeled source consists of a solid assembly. Thanks to specific expedients described in this chapter, the aggregation of single element-sources numerically equals the response on surface due to a cavity of the same shape with uniform pressure applied at the boundaries. A cost-efficient problem is, therefore, formulated to avoid unnecessary re-meshing procedures in favor of a model involving other levels of complexity and highly sophisticated. In the following paragraphs, we describe the characteristic of the FEM domain, built ad hoc for our original method, as well as the details about the elementary unit and the methodology we use to build the deformation source.

1.1. The Finite Element domain

The first step in the development of our approach is the creation of a three-dimensional Finite Element domain (Figure 3a). We use the MSC Marc/Mentat 2013 software to build a non-uniform mesh, consisting of 144.000 elements, of which nearly 10.000 constitutes a central regular portion (Figure 3b). In this portion, the elements are cubic and sized 400x400x400 m, occupying a volume of the mesh that extends laterally for ~16 km and until 15 km of depth. Our model solution is built in this volume (Figure 3c).

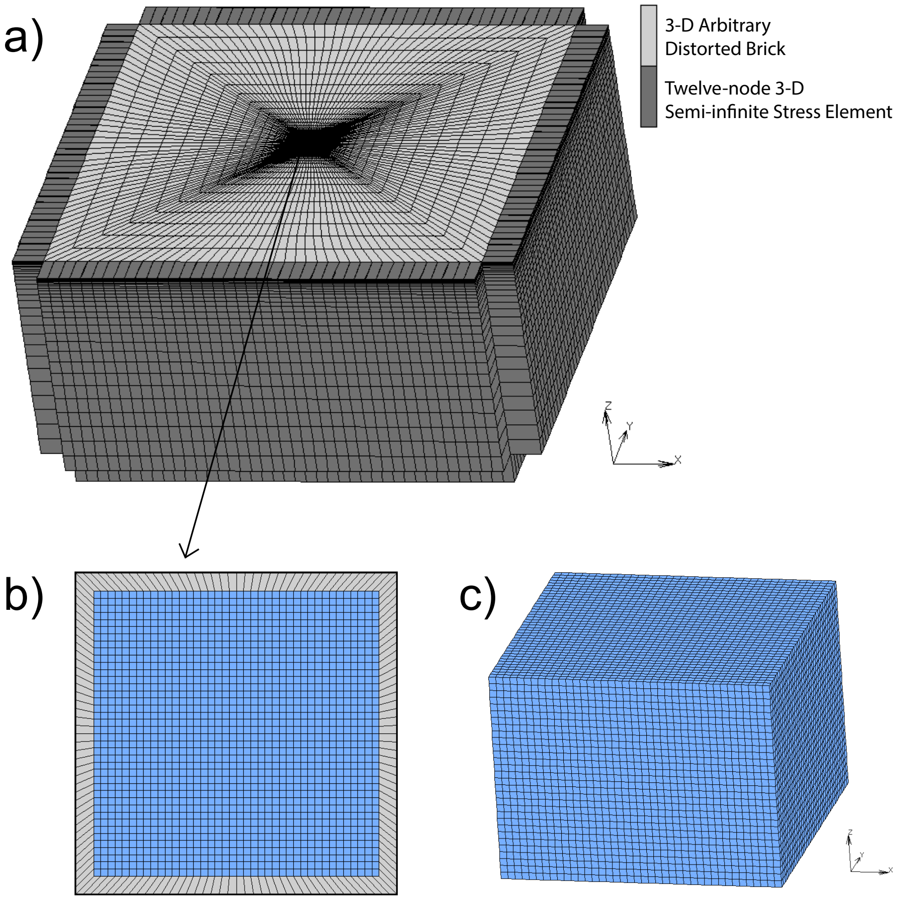

Figure 3. The Finite Element domain. a) Non uniform FE-mesh used in our approach with semi- infinite elements at the lateral and lower boundaries (dark grey); b) detail of the regular portion of the mesh grid; c) selected volume of cubic elements in the regular grid, used to model the deformation source.

This starting grid has been used for all the synthetic tests we present in the next chapters, but can be scaled and characterized ad-hoc by the user accordingly to the information available for the case study area where the model is applied. Therefore, as it is intended for the sole theoretical and methodological development purposes, we use a domain with a flat free surface and homogeneous elastic properties.

We set the material properties based on the literature, defining a Young's modulus of 2.5 GPa and a Poisson's ratio of 0.25. A study has been performed on the effects of different types of boundary conditions on the surface solution. The application of semi-infinite elements at the lateral and lower boundaries of the mesh (Figure 3a) is proved to be the best way to simulate an infinite crust and avoid boundary effects. We define, also, a set of surface element nodes (~4000), where the displacements solutions due to our source model are extracted by means of Python subroutines.

1.2. The elementary source unit

We design an elementary unit suitable to be assembled into aggregates with potentially any shape. A variety of configurations in the FEM have been tested such as, for example, a tensile opening acting on the centers of contiguous element faces patches at the source boundaries (Figure S1 in SM), simulating uniform pressure conditions. Although the efficiency of this method has been validated we discard this option for the high complexity, in favor of simpler and more versatile unit. In fact, we achieve our goal by loading the faces of a chosen number of cubic elements with a stress of 1 MPa. These elements belong to the regular central portion of the three-dimensional grid. In particular, by means of Fortran subroutines compatible with MSC Marc/Mentat software, we apply these stresses to each element in the form of the six components of a stress tensor (σ_{ij}), similarly to the approach of Trasatti et al. (2008). The six components are, namely, the three normal stresses (i.e. σ_{xx}, σ_{yy}, σ_{zz}) and three shear stresses (i.e. σ_{xx}, σ_{yy}, σ_{zz}), represented as combinations of dipoles and double couples of forces, as illustrated in Figure 4.

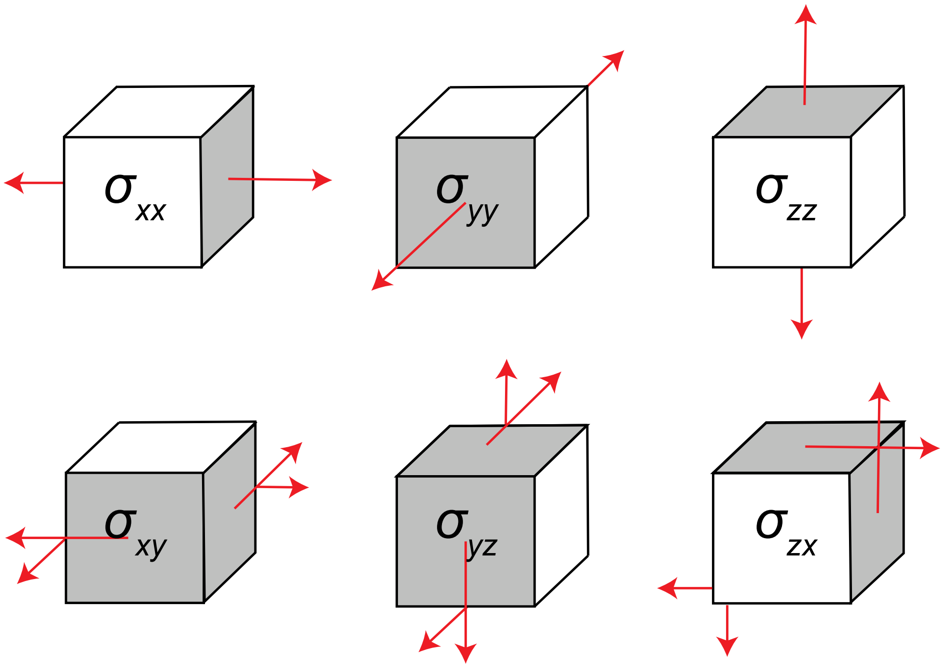

Figure 4. The Elementary source unit. The elementary unit mechanism consists in the application of dipoles and double couple of forces to the faces of a cubic element. These forces of 1MPa are applied as a unitary stress tensor.

We use, then, this source mechanism to reproduce the conceptual model illustrated in Figure 2, described in Yang et al. (1988) and Segall (2010), for which the deformation field of a pressurized cavity with uniform pressure applied to the boundary, is numerically equivalent to that of a uniform distribution of dipoles and couples of forces, appropriately scaled to respect the source aspect ratios relationships. We know, that the total deformation field (u_k) from the single element-source can be obtained by summing the surface responses of the six stress components ($u_{xx}, u_{yy}, u_{zz}, u_{xy}, u_{yz}, u_{zx}$), according to the superposition principle as in the following equation:

$$u_k(x, y, z) = s_{xx}u_{xx} + s_{yy}u_{yy} + s_{zz}u_{zz} + s_{xy}u_{xy} + s_{yz}u_{yz} + s_{zx}u_{zx} \qquad (1)$$

where, $s_{xx}, s_{yy}, s_{zz}, s_{xy}, s_{yz}, s_{zx}$ represent the scaling factors applied to each displacement solution, indirectly tuning the stress components magnitudes to obtain appropriate source mechanism.

In this study, we extend this concept to multiple elementary sources in an assembly, that constitutes our original source representation. We sum the contributions of each unit belonging to the source solution to obtain the total deformation field on surface, under the condition that the forces applied to each element must be identical, in order to reproduce the case presented in Figure 2. Therefore, we can define six uniform scaling factors to be applied to the sum of the surface responses from all the elements of the assembly. With this strategy, we are able to formulate a model solution of easy implementation, reducing the number of parameters to be estimated. For clarity, we summarize our technique in five main steps as follows:

1. We apply unitary forces of 1 MPa, in the form of six components of the stress tensor ($\sigma_{xx}, \sigma_{yy}, \sigma_{zz}, \sigma_{xy}, \sigma_{yz}, \sigma_{zx}$), to the faces of each cubic element in a chosen volume of the regular portion of the FE mesh grid.

2. The displacement at the surface due to each stress component applied to each element source is computed ($u_{xx}, u_{yy}, u_{zz}, u_{xy}, u_{yz}, u_{zx}$) and stored in a matrix of unitary solutions.

3. The contributions to each displacement solution from all the elementary units included in the source assembly are summed to obtain the total unitary displacements: $U_{xx}, U_{yy}, U_{zz}, U_{xy}, U_{yz}, U_{zx}$.

4. Six scaling factors ($s_{xx}, s_{yy}, s_{zz}, s_{xy}, s_{yz}, s_{zx}$) for the corresponding classes of total displacements are estimated to calibrate the magnitude of the forces applied to each elementary unit. Thanks to the applicability of the superposition principle and given the condition that all the units in the assembly have uniform stress

tensors applied, we are able to adjust the unitary solution a-posteriori, obtaining a deformation field that is numerically equivalent to that of a pressurized cavity (see Chapter 2 synthetic tests).

5. The displacement field due to the composite source is, finally, obtained as a linear combination of summed displacements and appropriate scaling factors, in a formulation similar to Eq. 1, as follows:

$$U_{tot}(x, y, z) = s_{xx}U_{xx} + s_{yy}U_{yy} + s_{zz}U_{zz} + s_{xy}U_{xy} + s_{yz}U_{yz} + s_{zx}U_{zx} \tag{2}$$

The validity of this approach is proved by an extensive collection of synthetic tests, illustrated in detail in the following chapter. We verify the numerical equivalence among the deformation fields produced by uniformly loaded elementary units in composite source configurations and those computed from equivalent cavities with uniform pressure applied at their boundaries. We perform in this way model benchmarking with both analytical and FEM cavity solutions in a comparative analysis.

Chapter 2

Benchmarking of synthetic source assemblies

In this chapter, we illustrate a selection of synthetic tests performed with the aim of benchmarking the proposed modeling approach. In particular, the surface response due to pressurized cavities with uniform pressure applied at their boundaries is compared with that of equivalent source assemblies loaded with appropriate stress tensors, following the methodology described in the previous chapter. We employ analytical source models proposed in the literature, providing solutions for cavities at depth in the elastic half-space with simple symmetric geometries. In addition, we create equivalent cavities in the Finite Element domain and apply normal pressures to their external faces, to fulfill the uniform pressure requirement. Thanks to this extensive testing phase we validate the robustness of our method, proving that the original source representation in a domain without cavities is suitable to reproduce correctly the deformation and stress feels of a pressurized cavity.

In the following paragraphs, the comparison of the deformation fields produced by sources with different geometries is presented. We start from the simple case of a spherical source, to spheroidal sources (with unequal axis ratios), both vertical and with dip and a strike angles, and finally a sill-like source. The different combinations of scaling factors, indirectly tuning the potencies of the forces applied to the elementary units in the source assemblies, are estimated for each test to reproduce the deformation field of the equivalent cavities. For this task we use a simple linear inversion based on the differential evolution (DE) method (Robič et al., 2005) implemented in Python SciPy package. We verify, for each test, that the principal moment values we obtain are consistent with the source axis ratios, according to Table 1 of Davis (1986).

2.1. The spherical source

The simplest test aims at reproducing the surface deformation field of a finite spherical cavity. In this case, we compute the horizontal and vertical displacements from a pressurized cavity using the McTigue (1987) analytical model function implemented in VSM software (Trasatti, 2022). This analytical model is described by five parameters in total: three parameters for the location of the source (i.e. x, y, z), the sphere radius (r), and the ratio between the overpressure (ΔP) and the rigidity modulus (μ). In addition, the solution depends on the Poisson's ratio of the medium (ν). We set these parameters to represent a spherical source at 7 km depth, with a radius of 1500 meters and fixing ΔP/μ and ν, respectively to values of 10^{-3} and 0.25 (Figure 5c). We create a cavity as well in the FE mesh by removing 203 elements in the regular portion of the grid, corresponding to an assembly shaping a spherical source equivalent to the analytical model, and we apply pressures of 1 MPa to the boundaries to simulate uniform pressure conditions (Figure 5b). Finally, we build our composite source in the domain without the cavity, according to the new methodology proposed in this thesis, loading the same 203 solid elements with unitary stress tensor components of 1 MPa (Figure 5a).

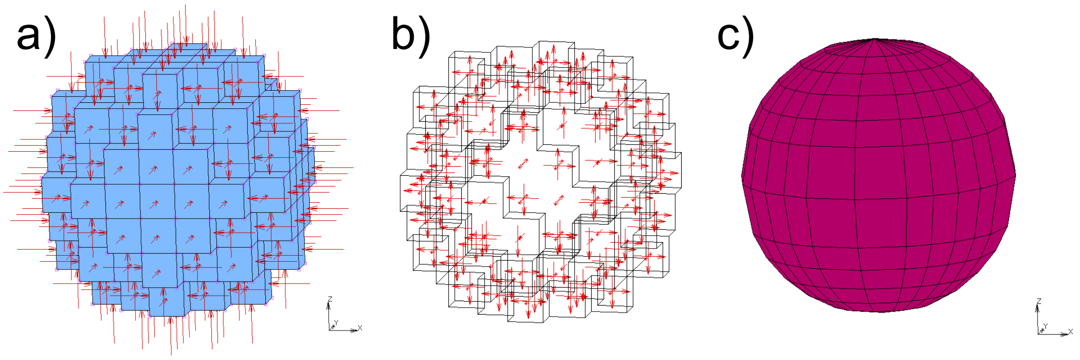

Figure 5. Spherical deformation source configurations. a) Solid assembly of elementary source units loaded with uniform stress tensors; b) spherical cavity obtained removing elements from the mesh and applying uniform normal pressure at the source boundary; c) analytical model for finite a spherical deformation source (McTigue, 1987).

We compute the displacements due to each source configuration at the location points corresponding to the set of surface nodes of the FE domain (see paragraph 1.1 in Chapter 1). We perform a comparative analysis of the deformation fields of both cavities (i.e. analytical and FEM) with our source assembly, scaling the six classes of unitary displacements, obtained from the sum of each elementary unit contribution, with appropriate factors retrieved by a linear inversion, as in the Eq. 2. As shown in Figure 6, we reproduce remarkably good the deformation field on surface of both cavities by scaling the displacements of our solid assembly.

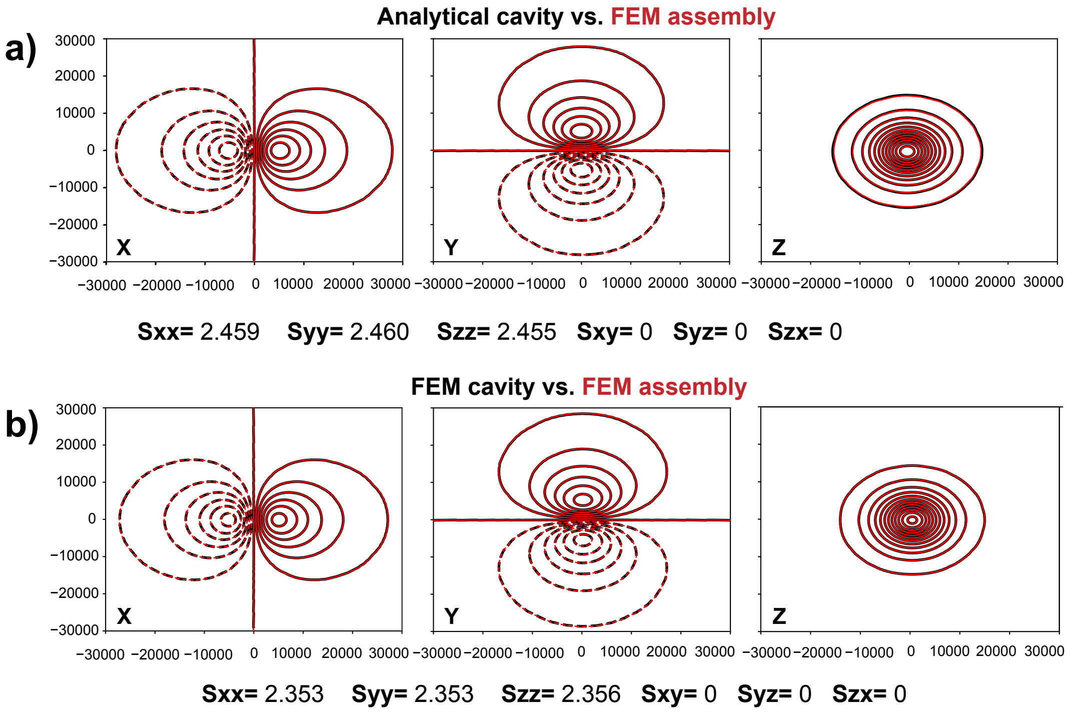

Figure 6. Comparison of deformation fields from a spherical source assembly using our method with relative scaling factors and those from equivalent pressurized cavities. a) Comparison between our source and the analytical cavity. b) Comparison between our source and the FEM cavity with uniform pressure applied at the boundaries.

We make use of only three stress components (i.e. $\sigma_{xx}, \sigma_{yy}, \sigma_{zz}$), as the source we model is isotropic and its orientation does not affect the surface response not requiring the shear stress components. We find uniform values for s_{xx}, s_{yy}, s_{zz} of ~ 2.46 to best fit the deformation due to the equivalent analytical source model (Figure 6a) and ~ 2.35 for that of the FEM cavity (Figure 6b). The misfit, in terms of minimization of the objective function approaches to zero in both comparisons (~1.2e-8; ~5.4e-10), with sub-millimeter displacement differences. Finally, the principal moment values are consistent with the relations existing among equal source axis, as in Davis (1986), where the spherical source is represented by three orthogonal dipoles of the same intensity.

2.2. The vertical spheroid

In the second numerical experiment, we test a prolate spheroidal source. In this case, the source shape is characterized by non-equal axis, with an elongation oriented in the vertical direction. We employ the analytical source model formulated by Yang et al. (1988) and implemented in VSM, which is described, as in the previous case by the three location parameters, the intensity ΔP/μ, but also by the length of the major semi-axis (a), the axis ratio (b/a) and the two orientation angles, dip and strike. We compute the surface displacement of a spheroid at 5 km of depth with a major semi-axis of 3000 m, avoiding the point-source approximation conditions (z/a ~ 1.7), and fixing the axis ratio to 1/3. As we aim at a vertical spheroid model, the orientation angles dip and strike are set, respectively, to 90° and 0°. A visual representation of the analytical spheroid is presented in Figure 7a. The equivalent FEM cavity is created by removing 179 cubic elements from the FE mesh and applying normal pressures to its boundaries (Figure 7b), while the same elements are used to build the source aggregate in the domain without the cavity, with unitary stress loads (Figure 7a), following the same procedure described in the previous paragraph.

Similarly to the previous test, the shear stress contributions are not required to reproduce the deformation field of the spheroidal cavities. The forces applied in the elementary source mechanisms are, in fact, represented only by the three dipoles of the normal stresses, since the source axes are oriented along the x, y, z directions.

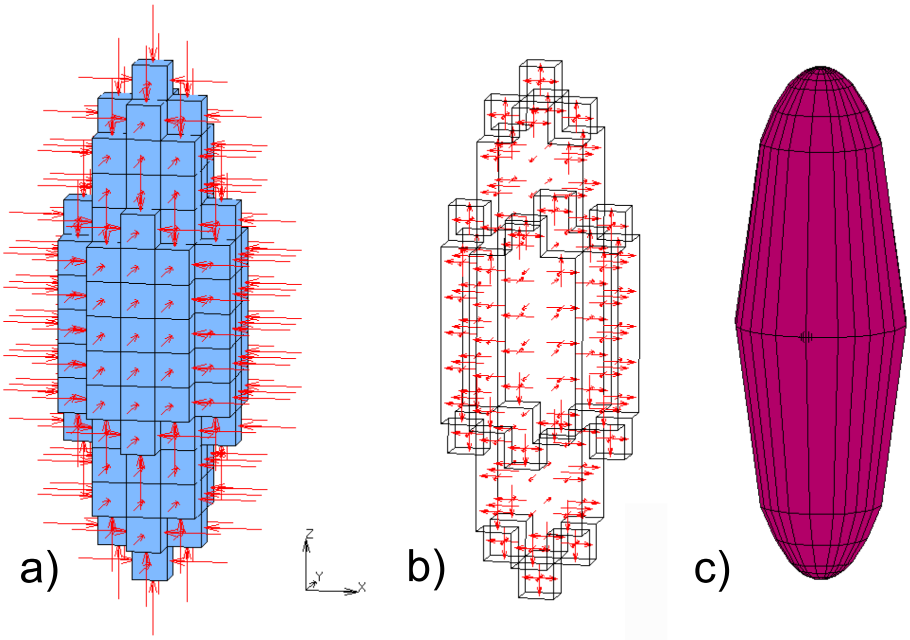

Figure 7. Vertical spheroidal deformation source configurations. a) Solid assembly of elementary source units loaded with uniform stress tensors; b) spheroidal cavity obtained removing elements from the mesh and applying uniform normal pressure at the source boundary; c) analytical model for vertical spheroidal deformation source (Yang et al, 1988).

We find the optimal values for the scaling factorss_{xx}, s_{yy}, s_{zz} respectively of ~2.86, ~2.86 and ~2.08, to fit the deformation field of the analytical solution (Figure 8a); while in the case of the FEM cavity, these factors are equal to ~2.77, ~2.77 and 2.04 (Figure 8b). In both cases, we notice that the forces applied along x and y directions (i.e. σ_{xx}, σ_{yy}) have a ratio equal to 1, while of ~ 0.7 for z/x (and z/y). These values correspond to the principal moment ratios proposed by Davis (1986) for a spheroidal cavity with axis ratios b/a = 1/3 and b=c, where a is the maximum semi-axis of the spheroid and b and c, the other two. We validate, then, our approach for the case of a non-isotropic geometry, being able to represent a vertical ellipsoidal source as an assembly of solid elements, loaded with an appropriate combination of forces, that numerically replicate the response due to cavities with uniform pressure applied at the boundary, just like in sketch proposed by Yang et al. (1988) and illustrated in Figure 1a.

Also in this case, the misfit approaches to zero in both comparisons (~6.9e-8; ~3.4e-10), with sub-millimeter displacement differences.

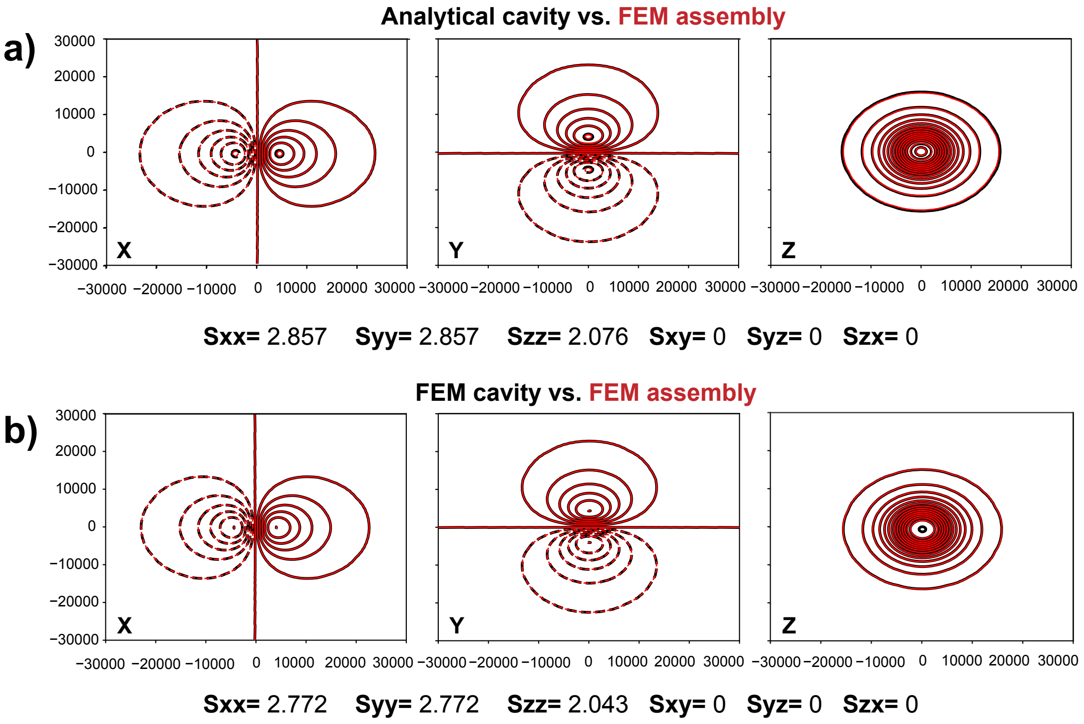

Figure 8. Comparison of deformation fields from a vertical spheroidal source assembly using our method with relative scaling factors and those from equivalent pressurized cavities. a) Comparison between our source and the analytical cavity. b) Comparison between our source and the FEM cavity with uniform pressure applied at the boundaries.

2.3. The spheroid with dip and strike

We now proceed to a higher level of complexity, testing the case of a prolate spheroidal source arbitrarily oriented in space. In this case, we use a dip angle ≠ 90° and a strike angle ≠ 0°, and this will lead to non-zero shear stress components $(\sigma_{xy}, \sigma_{yz}, \sigma_{zx})$ in the elementary source mechanisms, unlike the previous tests. We compute the deformation field due to an analytical pressurized cavity using the Yang et al. (1988) model. We set the length of the major semi-axis to 3000 m and the axis ratio to 1/3, as in the previous test, but we place the source at 9 km depth and fix the dip and strike angles, respectively, to 60° and 45° (Figure 9c).

An equivalent cavity in the FE domain is shaped by removing 187 cubic elements to the mesh and applying 1 MPa pressure at the cavity boundaries (Figure 9b). On the other hand, in the FE domain without the cavity, we load the same 187 elements with a stress tensor (Figure 9a) and we compute the total unitary displacements on the surface nodes of the grid due to the six stress tensor components.

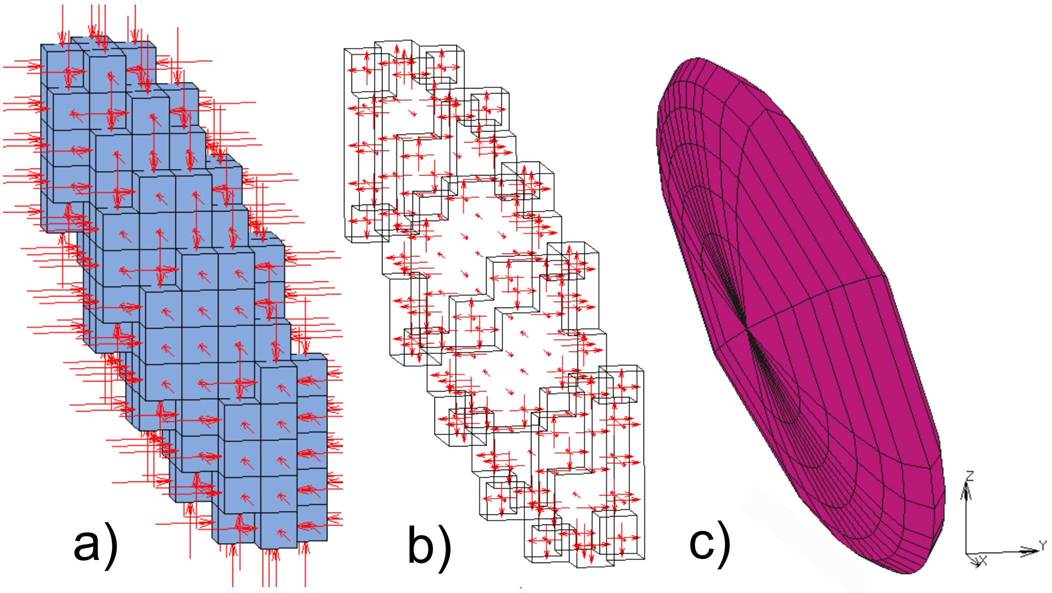

Figure 9. Inclined spheroidal deformation source configurations. a) Solid assembly of elementary source units loaded with uniform stress tensors; b) spheroidal cavity obtained removing elements from the mesh and applying uniform normal pressure at the source boundary; c) analytical model for inclined spheroidal deformation source (Yang et al, 1988).

The scaling factors for the unitary displacements referred to the source assembly, resulting from the inversion procedure to best fit the spheroidal cavities responses, are shown in Figure 10. We observe that, in this case, both normal and shear stress displacements are needed (Figure 10). This means that, the optimal elementary unit mechanism is a combination of dipoles and double couple of forces, differently from the tests illustrated so far.

We verify that the principal moment ratios of the stress tensor, defining the single element mechanism in the assembly, are consistent with those proposed by Davis (1986) for the same source we modeled.

Dedicated Fortran routines for the diagonalization of the stress matrix and interpretation of the principal values ratios based on Table 1 of Davis (1986) are employed, as in this case the analysis of the results is not straightforward. We verify that, in both cases, the relationships among the forces are consistent with the shape and orientation of the target source, according to Davis (1986). In fact, The resulting parameters are: b/ a=0.33 and c/a=0.33, dip=60.48° and strike=44.99°. The fit of the surface deformation is remarkably good in both the comparisons (misfit values respectively of: 1.3e-8 and 3.7e-10), proving that with our strategy we can model finite symmetric sources with any orientation in space.

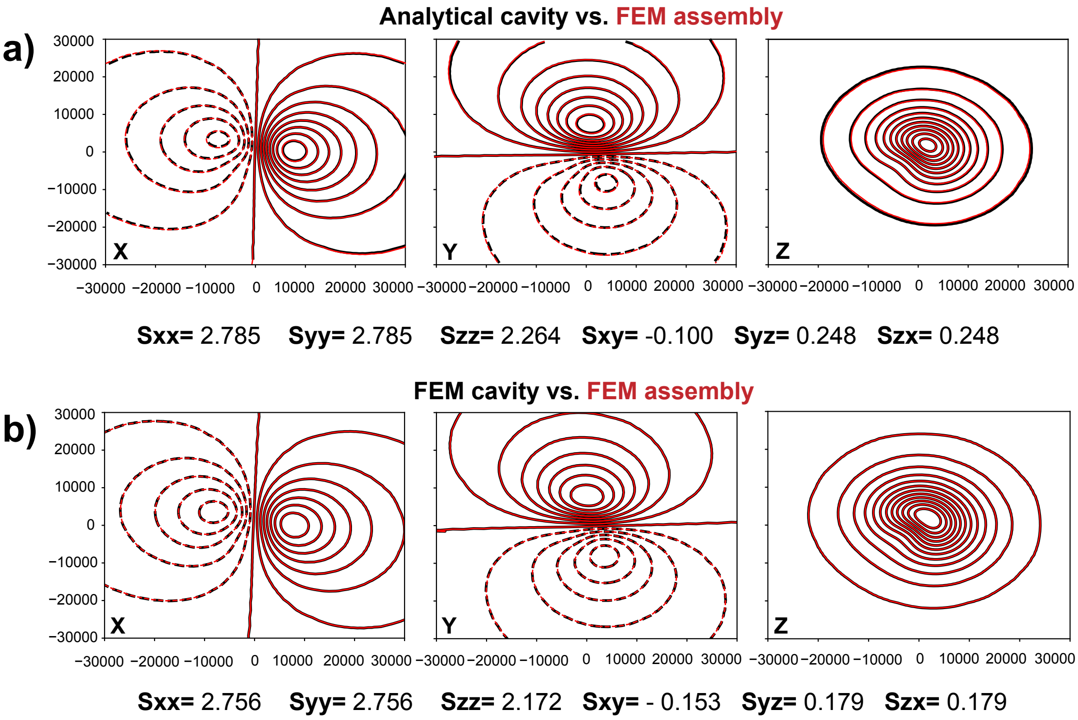

Figure 10. Comparison of deformation fields from an inclined spheroidal source assembly using our method with relative scaling factors and those from equivalent pressurized cavities. a) Comparison between our source and the analytical cavity. b) Comparison between our source and the FEM cavity with uniform pressure applied at the boundaries.

2.4. The sill-like source

The last test we present aims at verifying the equivalence of surface displacements due to sill-like sources, built in the three configurations illustrated in Figure 11. The goal is to reproduce the example presented by Segall (2010) and illustrated in Figure 2b, using our approach to distribute appropriate and uniform force combinations to simulate a pressurized cavity. Therefore, we first compute the response on surface with the analytical solution described in Fialko et al. (2001), employing the respective function from VSM software. The parameters describing this analytical model are the location of the source (i.e. x, y, z), the sphere radius (r), the ratio between the overpressure (ΔP), the rigidity modulus (μ) and the Poisson's ratio (ν) of the medium. We set the radius to 1400 m and the depth to 9800 m, while ΔP/μ and ν are the same of the previous tests (Figure 11c). The equivalent pressurized cavity in the FEM domain is created by removing 29 elements from the regular portion of the grid, in an assembly that shapes a horizontal penny-shaped cavity, and applying normal pressures on the faces at the cavity boundary (Figure 11b). Finally, the equivalent source as solid assembly is created by loading these same 29 elements with a unitary stress tensor, using the same procedure described in the previous paragraphs (Figure 11a).

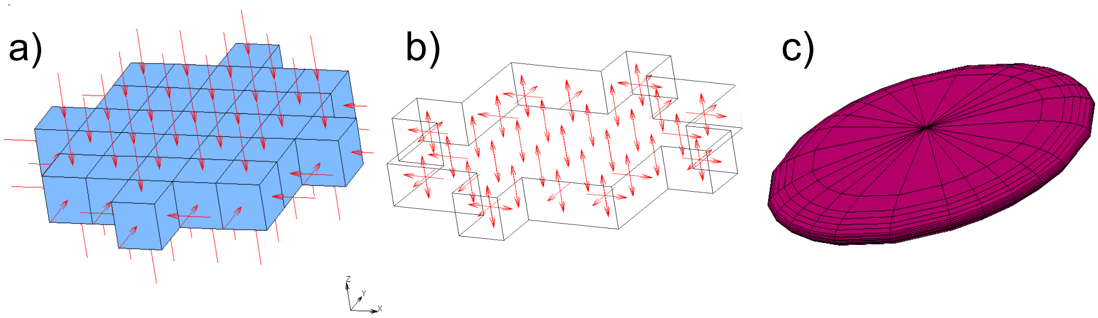

Figure 11. Sill-like deformation source configurations. a) Solid assembly of elementary source units loaded with uniform stress tensors; b) spheroidal cavity obtained removing elements from the mesh and applying uniform normal pressure at the source boundary; c) analytical model for penny shaped crack (or sill-like) deformation source (Fialko et al., 2001).

The sill-like model is horizontal, in fact, no strike and dip angles are foreseen in this solution, and it is symmetrical respect to the vertical axis. As in the case of the spherical source and the vertical spheroid, in order to fit the surface response of the analytical and FEM equivalent cavities, only the contribution from the three normal stress components are required. The best fit values for these parameters retrieved by the inversion code are shown in Figure 12. Again, we can reproduce the deformation field due to a sill-like cavity, scaling the displacements of an assembly of elementary sources using only three factors (see values in Figure 12). Misfit, as in all the test performed, is null (both cases ~1.1e-10). The deformation source model proposed in this work is, thus, extensively validated as a rigorous and cost- efficient strategy to simulate the most common settings of pressurized cavities at depth in FEM domains

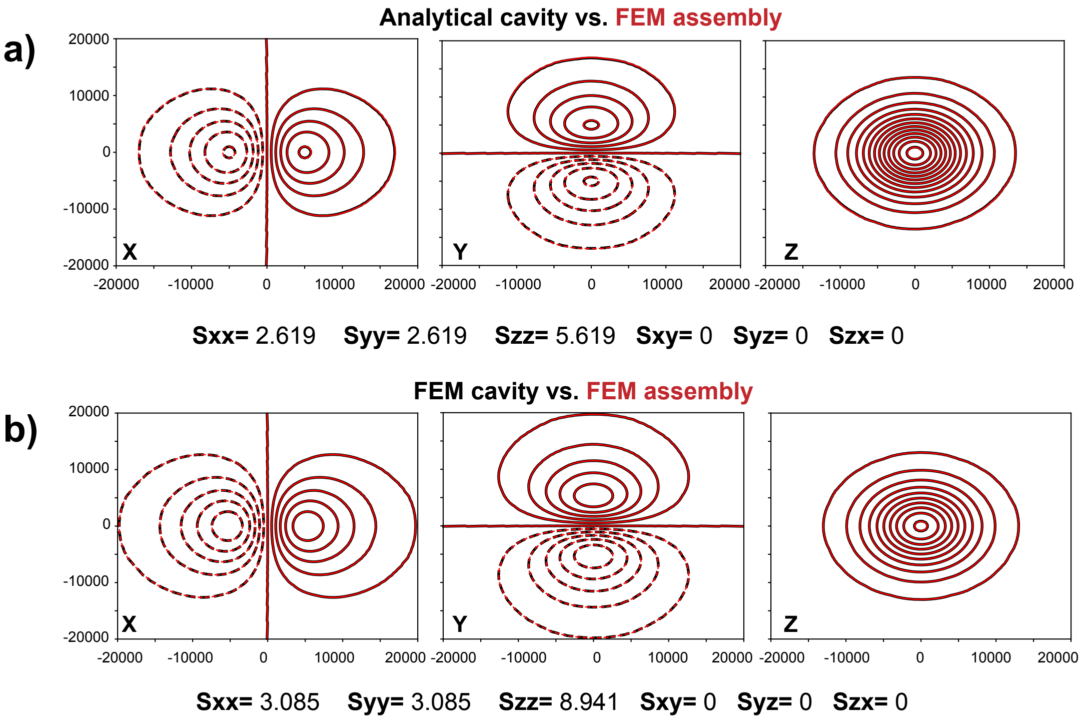

Figure 12. Comparison of deformation fields from a sill-like source assembly using our method with relative scaling factors and those from equivalent pressurized cavities. a) Comparison between our source and the analytical cavity. b) Comparison between our source and the FEM cavity with uniform pressure applied at the boundaries.

Chapter 3

The trans-dimensional inversion algorithm

In the previous chapters, we described our original forward model and its validation through synthetic testing with dataset from sources with known parameters, using models of pressurized cavities from analytical solutions from the literature and, also, built with FEM. The implementation of the new approach in an inversion modeling method is discussed in the following paragraphs. We present an original algorithm we designed ad-hoc for our problem, capable of shaping the deformation source assembly in the FEM domain based on the information provided by geodetic data.

As discussed earlier in this thesis, one of the key advantages that our method brings, is the possibility to pre-compute a library of displacements on surface for a volume of elements loaded with unitary stress tensor components, with efficient computational time of the inversion. In fact, as discussed earlier, we design a procedure that allows to adjust the forces applied to each the elementary unit in the source a-posteriori, scaling the displacements classes with uniform parameters. The matrix of unitary responses, computed for the elementary units in the portion of the domain where the source is expected to exist, on a set of surface nodes in the FE mesh, is provided as an input file to the algorithm.

During the inversion procedure an ensemble of solutions is formulated, defining simultaneously the assembly of elementary units and the appropriate scaling factors for the relative unitary responses. In particular, we use a Voronoi cells-based partition to sample the model space, implementing an innovative approach that foresees two competing sets of three-dimensional cells that determine which of the available element units belong to the source assembly and which to the inactive outer crust set. The numerical problem with an unknown number of parameters, i.e. the number of cells, is handled by a Bayesian trans-dimensional inversion approach of which we describe the main characteristics.

3.1. The Bayesian inference in inversion methods

In geophysics, the solution of inverse problems, that commonly consist in deriving models of the earth from surface observations, represents one of the main goals. This implies the use of mathematical relationships linking the data and the model, that for long time were based on simplistic assumptions and solved with linearized inversion approaches. With the advent of supercomputers and parallel computers a change towards highly sophisticated and CPU-time-consuming analyses has been experienced in the scientific field. Optimization processes in which the solution is presented as a single “final” best-fit model, can be replaced by probabilistic approaches, in which an ensemble of models is considered in comparison. This is the case of Bayesian inference algorithms, quantifying the information about the model parameters by their full posterior probability density distribution (PPD) (Tarantola, 2006). In particular, the objective is to investigate if and how the data provide additional knowledge to the a-priori information on the model parameters. Therefore, according to the Bayes’ rule (Bayes, 1763) the PPD is defined as:

$$p(\mathbf{m}\,|\,\mathbf{d},I) = \frac{p(\mathbf{m}\,|\,I)p(\mathbf{d}\,|\,\mathbf{m},I)}{p(\mathbf{d}\,|\,I)} \tag{3}$$

where, *p*() indicates a probability density and the conditional dependence, such as *A* given *B*, is written as *A*|*B*. The observed data (**d**), the prior information (*I*) and the model (**m**), appear in the notation of target PPD, i.e. $p(\mathbf{m}\ \ \mathbf{d},I)$, which is obtained as a combination of the prior knowledge of a given model, $p(\mathbf{m}\ \ I)$ with the likelihood of the model given the data, i.e. $p(\mathbf{d}\ \ \mathbf{m},I)$. Finally, the ‘evidence’ $p(\mathbf{d}\ \ I)$ represents the probability of the data in the model space computed used as a normalization factor for the PPD. Methods based on Markov chain Monte Carlo (McMC), exhaustively described in the next paragraph, do not require the evidence, that is a high-dimensional integral difficult to calculate.

These methods, are based on PPDs ratios from different models and allow to extract parameters information from the histograms of the sampled values, approximating the marginal probability density function (PDF), such as the mean and the standard deviation.

3.2. The Reversible-Jump McMC

Markov chain Monte Carlo (McMC) methods have been largely employed in inverse problems in geophysics to solve non-linearity and non-uniqueness, particularly in Bayesian frameworks (Sambridge & Mosegaard, 2002). In McMC algorithms, the direct computation of the analytic solution of Eq. (3) is replaced by the sampling of the model space with a random walk, according to probability rules (see Metropolis rule by Metropolis, 1953; described in paragraph 3.5.2) so that the chain of sampled parameters values is asymptotically distributed as in the PPD (Mosegaard & Tarantola, 1995).

We have seen (Chapter 2) that the number of model parameters in kinematic analytical models of deformation is constant. In the case proposed in this thesis, we use a workflow that does not require to fix the model dimension a-priori, since the number of model parameters varies during the iteration. In fact, the number of elements forming the composite source or, precisely, the number of Voronoi cells (see paragraph 3.3) containing these elements, is one of the unknowns of our model. We make use of an extension of McMC, known as reversible-jump McMC or trans-dimensional approach (trans-D) (Green, 1995; Denison et al. 2002), to invert for the number of parameters. This approach has been implemented in several geophysical problems such as, for example, resistivity tomography (Malinverno, 2002), seismic tomography (Bodin & Sambridge, 2009; Piana Agostinetti et al., 2015), and data-space exploration (Agostinetti & Sgattoni, 2021). By means of trans-D approaches the complexity of the model can be directly constrained by the data, avoiding a subjective smoothing, in a framework that is proven to be parsimonious, preferring simpler models rather than more complex ones, in accord to Ockham's razor logic (Malinverno, 2002). In addition, the level of detail of the solution is locally controlled by the data, thanks to an adaptive parametrization scheme (e.g. ,Voronoi cells, described in detail in the following paragraph). The model resolution is refined during the inversion process according to the quality of the data coverage (Sambridge & Faletič, 2003), obtaining a fully data-driven solution. A correct evaluation of data uncertainties is, therefore, crucial in trans-D sampling, since this method produces models whose complexity is consistent with the level of data noise. If the nature of the noise is not clear, a parametrization of the error would be appropriate. We employ a hierarchical Bayes approach, in which the standard deviation of the data errors (σ_{err}) is treated as an unknown parameter in the inversion process, following Malinverno & Briggs (2004).

3.3. Voronoi cells

In our inversion problem, we consider the Earth's crust as a discretized three dimensional domain in a FE mesh (see paragraph 1.1). In this domain, a volumetric deformation source is shaped as an assembly of elementary units, each one participating with its unitary contribution to the total surface response. Since the goal of the inversion is to find composite source configurations explaining the deformation we observe on the surface, we formulate a strategy to sample the available units, to identify which belong to the source and which to the embedding crust. We employ the Voronoi tessellation for this task, representing a way to divide a volume with non- overlapping, convex, polyhedral cells based on a distribution of points (e.g. Sambridge et al., 1995). These points represent the nuclei of the cells, i.e. Voronoi centers, while the edges of the cells are defined by the distance existing between them. In fact, a given point in the Euclidean space, belongs to the Voronoi cell having its center closer to this point than any other cell.

The resulting three-dimensional partition in our model is an ensemble of polyhedral cells built on our FE-domain, in particular, on the selected volume of element-sources for which we compute the solutions. Previous studies employed the Voronoi cells as a parametrization method in trans-dimensional algorithms, using them to assign Earth model parameters to regions of the model space (e.g. Malinverno, 2002; Bodin & Sambridge, 2009; Piana Agostinetti et al., 2015).

In our case, we formulate an innovative application of Voronoi tessellation, employing two different sets of competing cells to sample the model domain. One set of cells has the task of sampling the elements that form the source assembly and that contribute to the solution. The responses related to these elements are summed and scaled according to the method illustrated in the previous chapters, to compute the predicted observations of the composite source model. We will refer to this set, in the following paragraphs, as the set of Voronoi cells 'IN', as it samples the units that are inside the source. The second set, on the contrary, fills the remaining space in the three-dimensional model domain, where all the elements that remain inactive as part of the outer crust are localized. This set is, therefore, referred to as the OUT set of Voronoi cells, comprising all the elementary units that are left outside the solution. However, the role of the cells OUT is fundamental, as their distribution around the IN cells, defines the shape of the deformation source (Figure 13). In fact, by means of this strategy we can image volumetric deformation sources with potentially any shape, with geometries refined proportionally to the level of resolution of the data (e.g. data coverage, data accuracy). During the inversion process, the number and the position of Voronoi nuclei IN and OUT can vary, so does the model dimension in the RJMcMC. In this way a model is defined by a collection of both IN and OUT cells.

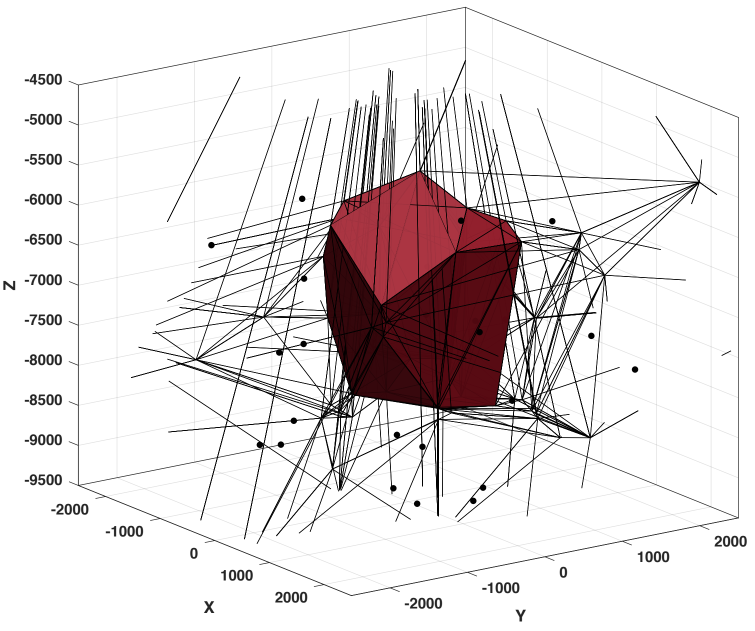

Figure 13. Three-dimensional model in terms of Voronoi polyhedral cells. Visual representation of the model domain sampled by two competing sets of cells: IN and OUT. In red, the ensemble of IN cells representing the deformation source; while OUT cells are represented by the black lines defining their edges and their nuclei (black dots) for a more clear visualization.

3.4. RJMcMC recipe

One of the fundamental ingredients of McMC based algorithms is the ‘recipe’, a list of moves that are defined to perturb the current model to produce a candidate, in the chain of models sampled during the inversion (Mosegaard & Tarantola, 1995). Our code is composed of 17 moves, designing a specific recipe for our problem. These moves are:

1. Perturbation of the scaling factor s_{xx} for displacements due to σ_{xx}.
2. Perturbation of the scaling factor s_{yy} for displacements due to σ_{yy}.
3. Perturbation of the scaling factor s_{zz} for displacements due to σ_{zz}.

4. Perturbation of the scaling factor s_{xy} for displacements due to σ_{xy}.
5. Perturbation of the scaling factor s_{yz} for displacements due to σ_{yz}.
6. Perturbation of the scaling factor s_{zx} for displacements due to σ_{zx}.
7. Perturbation of the standard deviation (σ_{errSAR}) of the InSAR data error.
8. Perturbation of the standard deviation ($\sigma_{errGNSS}$) of the GNSS data error.
9. Perturbation of the standard deviation (σ_{errLEV}) of the Leveling data error.
10. Perturbation of the position along x of one Voronoi nucleus IN.
11. Perturbation of the position along y of one Voronoi nucleus IN.
12. Perturbation of the position along z of one Voronoi nucleus IN.
13. Perturbation of the position along x of one Voronoi nucleus OUT.
14. Perturbation of the position along y of one Voronoi nucleus OUT.
15. Perturbation of the position along z of one Voronoi nucleus OUT.
16. Perturbation of the number of Voronoi nuclei IN.
17. Perturbation of the number of Voronoi nuclei OUT.

During the inversion, a perturbation according to one of these moves, randomly selected, is chosen. Each move is assigned with a prescribed probability that can defined by the user based on the prior knowledge or, when lacking of a-priori information is equally distributed among all the moves. Therefore, it is important to set the scale of the perturbation and the probability associated to each move, in a way that the parameter space is explored with a reasonable number of samples. In practice, if the perturbation is ‘weak’, a small change will occur from the current to the candidate model (see 3.5), then the new model will be likely accepted but the convergence will be reached in a longer time. On the contrary, ‘strong’ perturbations might result very inefficient, as the data fit would be likely worse, and the model would be not accepted, slowing down the chain convergence (Mosegaard, 2006). Several numerical experiments show that an acceptance probability equal to 0.25 maximizes the efficiency in the model space exploration (Gelman et al., 1996), therefore, is appropriate to set the recipe conditions according to this value.

The last two moves in the list, represent the trans- dimensional moves, controlling the dimensionality of the problem by adding or removing Voronoi cells, with the so called “Birth/Death” proposals (Geyer, 1944; Hawkins et al., 2019). Following the approach of Mosegaard & Tarantola (1995), a new cell nucleus is created at a random location foreseen in the prior distribution, or a random existing nucleus is removed by the model. We know from Mosegaard & Tarantola (1995) that, theoretically, different recipes can be employed for solving an inverse problem, as the Eq. 3 is independent from McMC characteristics, as it is based on the data and the prior information. This is true, under the condition that the proposed recipe fulfills the required probabilistic rules, as discussed in Sambridge & Mosegaard (2002). The recipe formulation has, nevertheless, an impact on the workflow efficiency, controlling the time required to adequately sample the PPD and so, to reach the convergence state.

3.5. Algorithm workflow and performances

In this paragraph, we illustrate in detail the algorithm workflow (Figure 14), based on a main loop implementing the McMC sampling. As previously mentioned, the algorithm reads different types of input files, including the observations, the pre-computed matrix of responses, relative to the elementary units selected from the FE-mesh, and the prior distributions of the model parameters. A starting model is randomly picked from the prior information (or specified by the user), and is perturbed according to the ‘recipe’. The perturbed model (i.e. candidate model) is accepted or rejected, becoming the new current model or not. A sequence of models are sampled and stored to define the PPD. The output files are collecting the information about the process and can be analyzed to extract the final results.

3.5.1. Model inputs: Data, Responses and Prior

In this paragraph, we start with a description of the input files we must provide to the code, before starting the inverse modeling procedure.

First of all, a geodetic dataset is required, containing the observations about the deformation field we want to model. The algorithm allows for different type of data, derived from the most commonly used techniques (i.e. InSAR, GNSS and leveling) performing a joint inversion. These data files must be adapted to the required format, as shown in Table 1.

In the case of InSAR data, multiple files from different orbits (i.e. ascending or descending) and different satellites can be handled. The use of observations from different geometries of acquisition is recommended, as it helps to approach a more accurate three dimensional representation of the displacement field. The unit vectors related to the sensor Line-of-Sight (LOS) must be specified at first.These three values, one for each direction, can be computed from the radar incidence (θ) and heading (ϕ) angles using the equations:

$$LOS_E = -sin(\theta)cos(\phi) \tag{4}$$

$$LOS_N = sin(\theta)sin(\phi) \tag{5}$$

$$LOS_Z = cos(\theta) \tag{6}$$

In addition, the statistics model associated to the error (i.e. exponential or gaussian), the correlation length of the data point, and the number of points can be specified. The data are accepted as LOS velocities, with the relative standard deviations. The GNSS data must be reported in the files, one component per row, assigning an index to each row that corresponds to East, North or uplift (Table 1).

Table 1. Supported format for data files.

InSAR				
LOS E [a]	LOS N [a]	LOS Z [a]		
Error statistics model [b]				
Correlation length [c]				
N° data points				
Easting [d]	Northing [d]	Data	Error	
GNSS				
N° data points				
Error statistics model [b]				
Easting	Northing	Data	Error	Component Index [e]
Leveling				
N° data points				
Error statistics model [b]				
Easting	Northing	Data	Error	

[a] *Columns LOS are the Line of Sight unit vector components.*

[b] *Index for the error statistics model: 0 = exponential, 1 = Gaussian.*

[c] *Correlation length of data points value between 0 and 1 (0 = uncorrelated)*

[d] *Geographical coordinates projected in meters*

[e] *Index for the velocity component: 0 = East, 1 = North, 2 = Uplift*

The second category of input files, includes the matrix of pre-computed responses from a selected number elementary units, with 1 MPa loads applied in the form of the six components of the stress tensor (see Chapter 1). This matrix will be used in the algorithm as the forward solver **G**(**m**). These responses are extracted for a given set of points, corresponding to the FE mesh surface nodes. The structure of this matrix is complex, as the rows are organized in Nx6, where N is the number of elementary units for which the responses are calculated six times, one for each stress component; while the columns are Mx3, corresponding to the three horizontal (x,y) and vertical (z) displacements each computed on M surface nodes. To allow the algorithm to interpret this matrix, two additional files are provided: one file with the number and the locations of the surface nodes, on which the solutions are extracted, and one file with the number of elementary units, their identification number and the location of their centroids. Finally, the prior information must be defined as probability density distributions representing our initial state of knowledge about the model parameters. The prior distributions of our model parameters are all uniform over a range set by the user. Therefore, the minimum and maximum number of Voronoi cells IN and OUT, as well as the limits of the three-dimensional volume in which the Voronoi cells nuclei can be located, the range of values for the scaling factors for the six displacements classes and for data error, are listed in an input file.

3.5.2. The main loop: Candidate model and Metropolis' rule

As illustrated in Figure 14, the core of the algorithm is the McMC sampling, operating with an iterative process, in which a sequence of models are sampled following this logic:

1. After reading the input files, the algorithm creates a random starting model based

on the prior distribution ranges. This model is the first ‘current’ model $(\mathbf{m}_{curr})$ of the McMC chain.

2. The current model is perturbed with a random move, according to the probability defined in the recipe. The perturbed model is, therefore, recognized as the ‘candidate’ model $(\mathbf{m}_{cand})$,

3. The predicted observations associated to the candidate model are computed and so its likelihood function $p(\mathbf{d}\ \ \mathbf{m}, I)$. The likelihood is a way to measure the fit of the predicted data respect to the observed, based on a simple least squares misfit. The general likelihood function is formulated as follows:

$$p(\mathbf{d}\,|\,\mathbf{m}, I) = \frac{1}{((2\pi)^{N_d}|\,C_{err}\,|)^{\frac{1}{2}}} e^{\frac{-\phi(m)}{2}} \qquad (7)$$

where, N_d is the number of data points, C_{err} is the covariance matrix of the errors, ϕ represents the difference between the predicted and the observed data, and

is defined as:

$$\phi(\mathbf{m}) = (\mathbf{d} - \mathbf{G}(\mathbf{m})^{\mathbf{T}}\mathbf{C}_{\mathbf{err}}^{-1}(\mathbf{d} - \mathbf{G}(\mathbf{m})) \qquad (8)$$

where, $\mathbf{G}(\mathbf{m})$ is the forward solver, that in our method is pre-computed as the matrix of unitary responses The covariance matrix C_{err}, is referred to errors of different nature. If we assume that these errors are uncorrelated (correlation length set to zero), we also imply that they all share the same standard deviation σ_{err}, foreseeing a diagonal covariance matrix. This assumption is commonly adopted in modeling approaches with the aim of simplifying the computation, whereas our code offers the option to consider a grade of correlation for a more sophisticated analysis.

4. The acceptance or rejection of the candidate model ($\mathbf{m}_{cand}$) as the new current ($\mathbf{m}_{curr}$) is based on the Metropolis-Hastings algorithm (Metropolis et al., 1953; Hastings 1970). The acceptance probability is defined by the ratio between the likelihood computed for the candidate model and for the current model, as:

$$\alpha = min\left[1, \frac{p(\mathbf{d}\,|\,\mathbf{m_{cand}}, I)}{p(\mathbf{d}\,|\,\mathbf{m_{curr}}, I)}\right] \tag{9}$$

   According to this probability, if the likelihood of the candidate model is higher than that of the current model, the model is accepted with a probability equal to 1, otherwise, the model is accepted with the probability equal to the value of (can be rejected if =0). If accepted, the candidate model ($\mathbf{m}_{cand}$) becomes the new current model ($\mathbf{m}_{curr}$), otherwise the current model is kept. The the chain starts a new loop until the steps reach the number of iterations defined by the user.

5. The sampled models are stored and participate to the PPD distribution, representing the final output of the inversion.

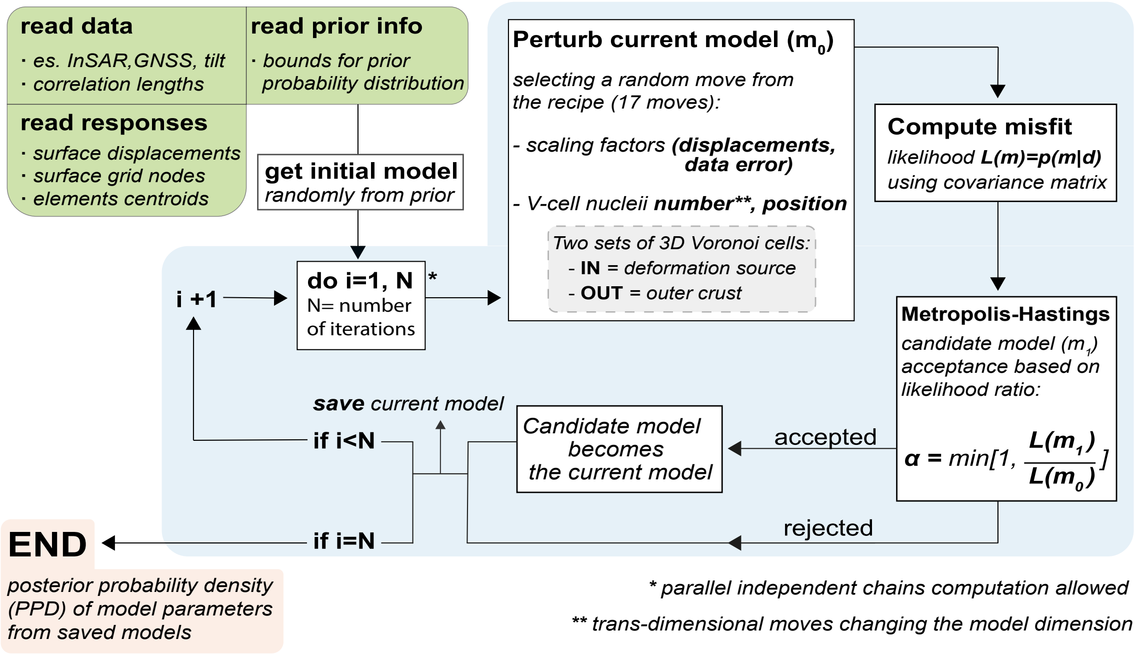

Figure 14. Flowchart describing the main loop of the inversion algorithm. In green, input files that are read by the code. The initial model is perturbed as illustrated in blue, according to the probability of each move. The new candidate model is accepted or rejected based on the likelihood as in Metropolis-Hastings rule. The current models are stored to build the PPD (red box). The loop ends when the number of models defined a-priori by the user has been created.

3.5.3. Model outputs

The algorithm creates several output files, in which all the informations about the simulation are kept for post-processing and interpretation of the results. In particular, the output files produced for each chain are:

- One file containing information about the starting model for a given chain.
- One file with the chain sequence details (e.g. type of move, acceptance info, likelihood computed for candidate and current model, number of cell IN and OUT).

- One file reporting the parameters for each sampled model such as: the Voronoi nuclei coordinates, the values of the scaling factors of the six displacements and the data errors, the number of elementary sources included in the cells IN.

- One file with the moves statistics.

The ensemble of models stored are distributed according to the posterior probability density function (PPD). From the distribution of the PPDs of the model parameters we can extract the mean values and the standard deviations associated. Three dimensional plots of the Voronoi diagram based on the distribution of the cells nuclei allows for a visualization of the source shape. The predicted data can be computed for a model with the mean parameters extracted from the PPDs, or for any model.

3.5.4. Performances

The code presented in thesis is developed using FORTRAN programming language for its best performances in terms of CPU time. We account for the possibility of using high performance computers (HPC), allowing the use of multiple independent McMC chains (ideally one for each CPU available in a cluster) for an exploration of a larger portion of the model space and shorter chains. In general, we observed that the number of models required to reach the convergence state is in the order of 10^5. The computation time required depends, in part, on the number of datasets included in the inversion, as well as on the computer performance. We run for our tests, averagely, a complete inversion with two InSAR datasets and 10^5 models per chain in ~2-3 hours, a more than sustainable time for a numerical modeling approach of this complexity. These simulations are performed on Ing580 machine (four hex-core processors) and other computational resources from Istituto Nazionale di Geofisica e Vulcanologia. Further enhancements of the algorithm performances can be done, e.g.

increasing the model sampling interval in the output files. As discussed in the final paragraphs of this thesis, as we foresee the use of large datasets to fully exploit the RJMCMC potential in terms of model resolution, a more sophisticated structure in the parallelization is planned, consisting in a master/slave approach (Mandolesi et al., 2018). This approach is based on a master chain defining the jobs for a number of slave CPUs, in our case distributing the computation of the synthetic responses, the heaviest part of the algorithm workflow.

Chapter 4

Algorithm validation through synthetic tests

In this chapter, we give a practical example of the inversion procedure, with a one representative test performed for code debugging and validation. We highlight the capacity of our code to deal with a complex problem and solve it following the principle of parsimony. In fact, we observe that along the sequence in the McMC chains, although the misfit has already reached a steady state value, the algorithm continues to sample models with a decreasing number of cells to assess the dimensionality of the problem (i.e. the number of parameters). In addition, we illustrate how the two sets of competing Voronoi cells interact in the model domain partition. The use of two trans-D elements in a reversible jump McMC algorithm is an original characteristic of our approach, that we conceptualized ad hoc for our problem. Our tests follow the same logic of those proposed in Chapter 2, as we compare the deformation fields due to different source configurations. We pass, in fact, from the assembly of elementary units in the FE domain, to an equivalent source sampled by a given distribution of Voronoi cells IN and OUT. We create noisy synthetics with our algorithm, defining the Voronoi cells nuclei that shape the target source and we let the inversion code retrieve a solution with simpler configurations of cells. Even if a more extensive testing and simulation would be appropriate to fully investigate the code potential and logic, we are already able to draw attention on the promising characteristics of the algorithm, that provide new insights for trans-dimensional algorithm applications.

4.1. From analytical to V-cells source representation

As anticipated in the previous paragraph, a testing phase of the algorithm has been carried out, since the level of sophistication we foresee and the innovative trans-D applications requires refinement and investigation. We present here a selected example of a practical inversion process.

We analyze the outputs from a test aimed at retrieving a vertical spheroidal source at depth. This target source is equivalent to an analytical vertical spheroid (Yang et al., 1988) with semi-major axis (a) of 1500 m, b/a (or c/a) ratio of 0.5 and $\Delta P/\mu$ of 10^{-3} and 0.25 (Figure 15a). The source assembly to retrieve is formed by 30 cubic elementary units (Figure 15b) sided 500 m, loaded with only the three force dipoles corresponding to the normal stresses (see 2.2). The scaling factors (s_{xx}, s_{yy}, s_{zz}) for these components are, respectively, 2.57, 2.57 and 1.99. The synthetic source used to compute the surface observations to be inverted is created using our algorithm. We define IN and OUT Voronoi cells nuclei sampling the same 30 elements of the target source, in a way that the IN cells boundaries correspond to the faces of the cubic elements (Figure 15c). We place, therefore, the cells nuclei at the elementary unit center locations of the 30 elements in the assembly for the cells IN, and of the 50 surrounding elements for the cells OUT.

The inversion is performed to find the simplest models configurations explaining the data, in the way illustrated in the example of Figure 15d. The model reported is an ideal solution, by way of an example, that samples the 30 elements of the synthetic source with a reduced number of cells (a single IN cell at the center of the source and 14 OUT), keeping the model dimension small. All these sources produce the same deformation field at the surface, validating our approach.

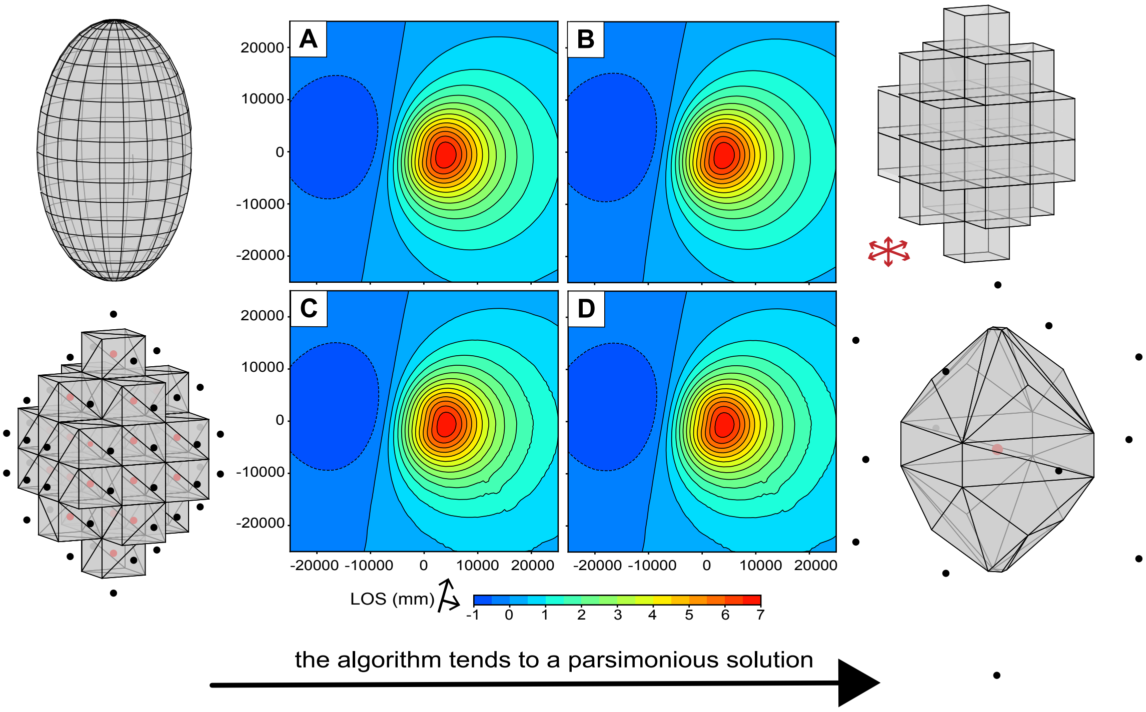

Figure 15. Comparison of source configurations following the logic of our tests. a) analytical pressurized cavity (Yang et al., 1988); b) assembly of elementary source unit loaded with an appropriate stress tensor; c) source assembly in terms of V-cells used to compute the synthetic data; d) example of an ideal solution after the inversion, sampling the same units of c with less cells.

4.2. Data and fit

We compute synthetic data with our algorithm from the source configuration of Figure 15c. The data are obtained in the form of InSAR LOS displacements from an ascending orbit with unit vector values of, respectively, 0.67, -0.11 and 0.72. We define a non uniform grid of data points, more dense at the center of the grid and more sparse in the far field, with a total number of 887 points. For a better visualization, in Figure 16, we interpolate these points on the surface grid of nodes of the FE mesh (4249). Gaussian white noise with zero mean is applied to the synthetic data as shown in Figure 16b.

An example of predicted data is shown in Figure 16c, using the last sampled model of one of the 20 independent chains, characterized by the lowest value of misfit. The comparison highlights that the predicted data from the model are nearly identical to the observations. The maximum LOS displacements is

~0.007 m for data and predicted.

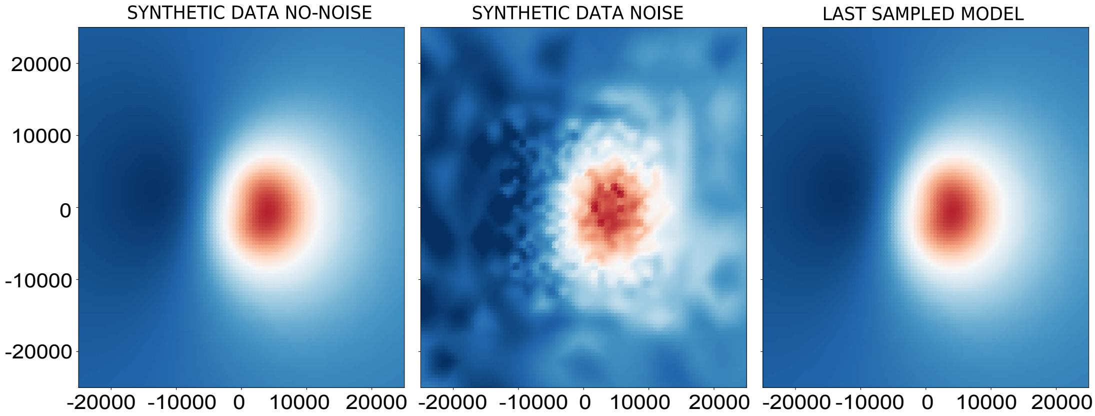

Figure 16. Comparison of observed and predicted data. a) Synthetic data computed as ascending orbit LOS displacement without noise; b) noisy synthetic observations; c) predicted data from a selected model sampled at the end of a McMC chain.

4.3. Voronoi cells sampling of the model space

In this paragraph, we illustrate how the sets of Voronoi cells works for sampling the model domain. The combination of cells IN and OUT, in fact, defines the region of the domain representing the deformation source, namely, the ensemble of 3D IN cells shaped by the OUT cells position (Figure 13, 17). The IN cells englobe a number of elementary sources that concur to the model solution, as the sum of their contributions gives the total displacement field (see Chapter 2). We initialize the test inversion, starting with a given initial model, described by a combination of 418 OUT cells, having their nuclei at the centers of the elements located at the extremes of the volume we considered as the model space, while a single cell IN center of the target source (coordinates: 0, 0, -7250 m) is considered.

To reduce the computational time we perform our test using a subsample of elementary units (~1000), in a volume ranging between -2500 m to 2500 m along X and Y directions and between -4500 m and -9500 m along Z (Figure 17). During the inversion, the number of cells and their positions can be perturbed according to section 3.5.2, changing the source shape.

An example of the model solutions is provided in Figure 17, consisting of the last sampled model of the chain showing the lowest misfit at the end of the test inversion (16000 samples). Only the surfaces of the IN polyhedral cells are drawn in grey, omitting those of the OUT cells and showing only their nuclei distribution, for a more clear visualization. This ensemble of two IN cells approximates the vertical spheroidal source, although longer chains would be appropriate and spatially denser data, for a better refinement of the shape. We are able, nevertheless, with the presented results, to show that our innovative approach, based on competing cells, is suitable to sample the model domain, solving for deformation sources free of shape constraints.

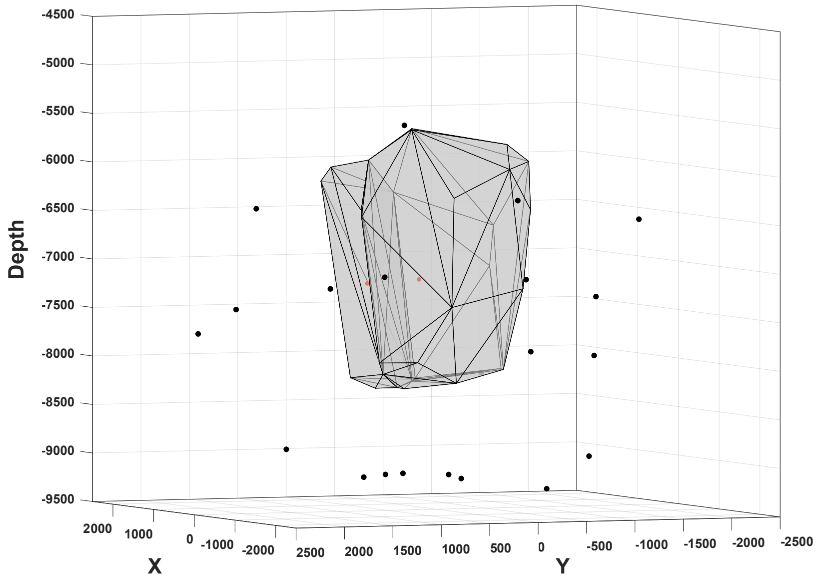

Figure17. Three dimensional plot of a source model. The surface of the Voronoi cells IN is drawn in grey. The source shape is depending on the position of the Voronoi cells OUT nuclei and their surfaces. In this figure the edges and faces of the polyhedral OUT cells are omitted.

Moreover, an analysis of the sampled elementary units, based on the last models stored in each of the 20 independent McMC chains, gives an idea about the capacity of the inversion to locate the source in the correct portion of the model domain. We can highlight that the most sampled elementary units are those we used to build the synthetics (Figure 18). The elements that are sampled fewer times and that are not belonging to the synthetic source, on the left and right extremes of the plot, are contiguous to the synthetic assembly. This is an expression of the solution variability that is controlled, mostly, by the resolution power of the observations. In particular, we notice that two elements belonging to the synthetic assembly are not sampled almost at all, which are identified by the IDs 383 (0, 0, -5750) and 428 (0, 0, -8250). These elements IDs correspond to the two element at the top and bottom tip in the assembly, likely meaning that the data are blind for this level of detail, as they their contribution to the predicted data is negligible, or null (see fit Figure 16c).

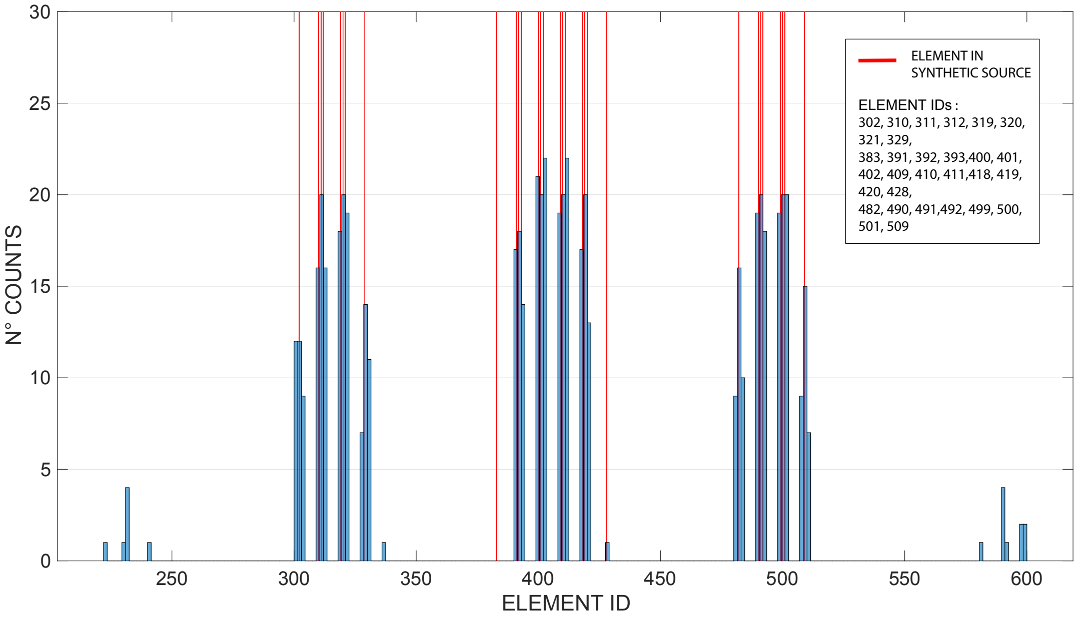

Figure 18. Histogram showing the sampled elementary sources in the last models of the chain. We show the counts of sampled element units in the ensemble of the last model of each chain. In the box the IDs identifying the elements that are used to build the synthetic source assembly, highlighted by the red lines. These elements are the most sampled, except 383 and 428, that are probably not resolved by the data.

4.4. Misfit and parsimonious solutions

One of the key characteristics of our algorithm, related to the use of reversible jump McMC, is that it tends to estimate the solution without introducing unnecessary details. In this section, we demonstrate that the inversion progressively discards solutions characterized by an overcomplexity, tending to the smallest problem dimension for the same model misfit. In the graph presented in Figure 19, we plot the trends of the likelihood values for the current models sampled by the 20 chains. We observe that the misfit decreases quickly during the inversion, reaching a stationary value after few hundred models for the test we propose. Typically, the steady value of LPPD0 approximates that of the data points, in this case amount to nearly ~900. The stage when the misfit values are stable is the convergence point of the inversion.

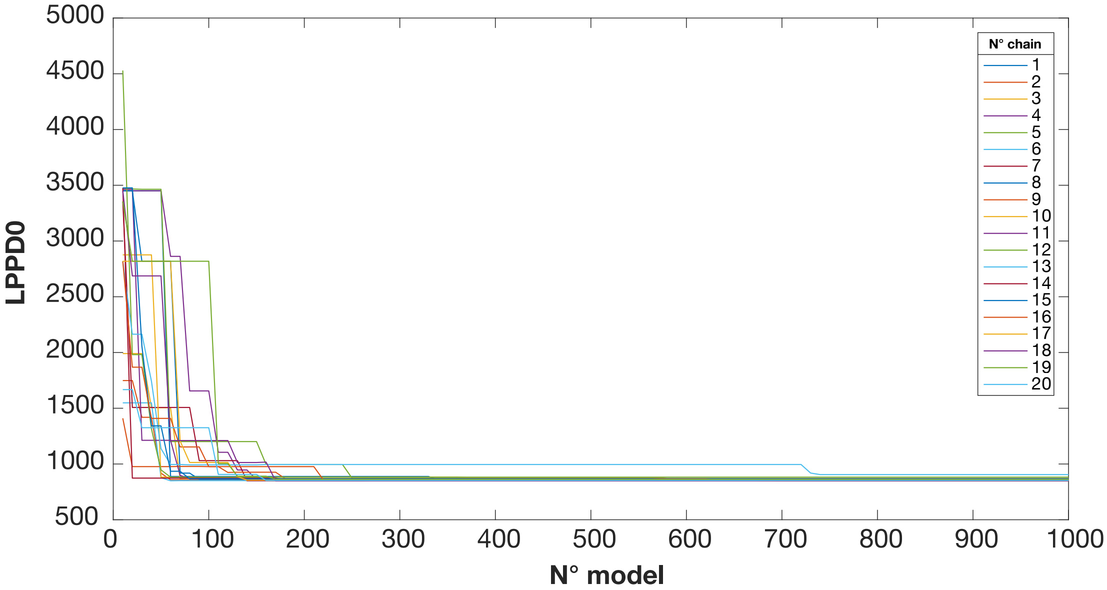

Figure 19. Misfit trends for the 20 independent McMC chains. The misfit, defined in terms of likelihood of the current models, decreases quickly in all the chains. After few hundreds samples the misfit reaches stationary values approximating the number of data points.

We observe that our algorithm continues to enhance the solutions in terms of complexity, even if an optimal misfit value has been reached. This is evident from the comparison of the misfit convergence plateau starting from 200-300 models in Figure 19 and the trends in Figure 20, describing the number of Voronoi cells in the models sampled by each chain. In particular, the plot shows the number of Voronoi cells OUT trends, highlighting that a consistent decrease in the number of cells occurs throughout all the chains sampling sequences. Simulations verify that all the trends, at one point, asymptotically lie on the lowest possible number of cells nuclei OUT that are necessary to constrain the source shape. An example of model result is represented by the source in Figure 18, that produces the deformation field on the surface in Figure 16c, being the last sampled model of the chain with the lowest misfit. This model is described by 2 IN cells and only 22 OUT cells, against the 418 OUT cells of the initial model. We conclude that the algorithm is operative and that owns specific features that might open the ways to a number of applications and further developments.

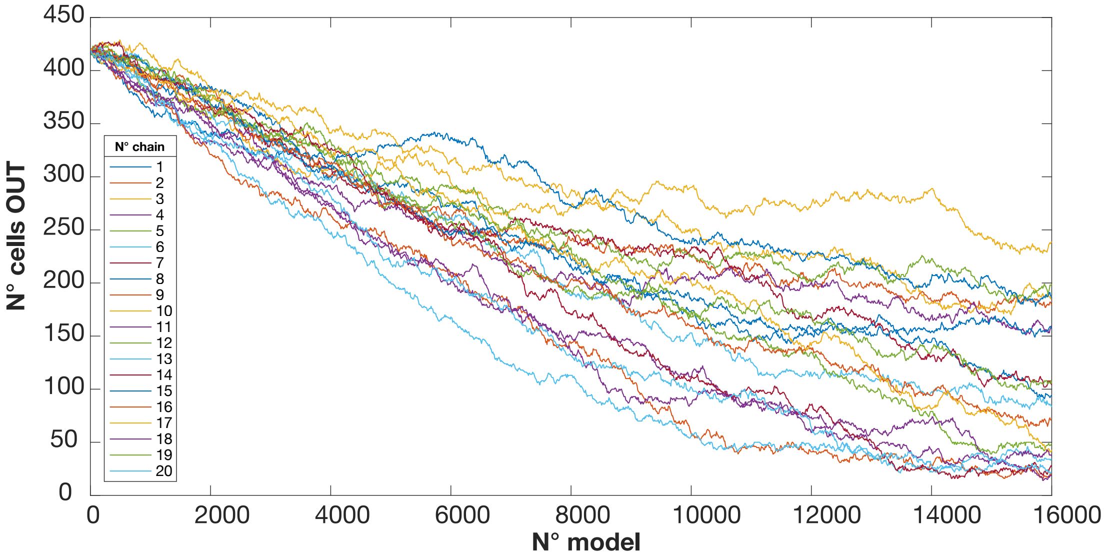

Figure 20. Number of OUT cells trends for the 20 independent McMC chains. In this plot, the decreasing trends represents the numbers of OUT cells in the sampled models, highlighting the algorithm tendency to reduce the problem dimension. All the chains starts from the same initial point (418 OUT). The simulation we show requires more samples to reach the convergence.

Chapter 5

The Long Valley caldera case study

We present in this last chapter a study about Long Valley caldera, in California (USA), that we chose for the application of our new modeling method. This volcanic site is one of the most studied worldwide, therefore, an extensive literature and variety of dataset are available for our implementation (e.g. Battaglia et al., 2003). The Long Valley caldera is in an unrest phases since 1979, experiencing since then episodes of seismicity and ground deformation, occurring in the area of the resurgent dome inside the caldera (Hill et al., 2020). The last inflationary trend started in 2011 and continued for more than a decade (Montgomery-Brown et al., 2015). We collect and process geodetic data that fully cover the period from 2011 to the end of 2021. In particular, we produce Interferometric Synthetic Aperture Radar (InSAR) data using different satellite sensors, i.e. TerraSAR-X (TSX), COSMO-SkyMed (CSK) and Sentinel-1 (S1), with different acquisition geometries and operating with X and C-bands, to increase the accuracy in mapping the deformation. Also, we use GNSS velocities from the monitoring network of the California Volcano Observatory. We correct for tectonic, hydrological and seismic contributions to the displacement field to derive the signals caused by the caldera dynamics. With our dataset, we are able to investigate the characteristics of the deformation source at depth by means of inverse modeling. In particular, we employ the moment tensor source model (Davis, 1986) to retrieve the relationships among the principal moment values, describing the source and infer the source geometry. These results are preparatory for the application of our modeling approach, based on the moment tensor application. Our findings show that the source can be represented as a nearly vertical spheroid, having a shallower depth in the second half of the period analyzed. This result is consistent with previous studies and the modeling of the previous unrest in 1988-1999 we additionally performed.

5.1. Introduction

The Long Valley Caldera (USA), located in Eastern California, experienced in the last decades unrest phases with seismic swarms and ground uplift. The ground inflationary trends were observed in the central caldera, near the resurgent dome area (Figure 21), characterized by a nearly axisymmetric tumescence (Montgomery et al., 2015; Hill et al., 2020). The highest rates have been recorded in 1997-1998, when nearly 10 cm of uplift occurred (Battaglia et al., 2003; Langbein, 2003), while the last deformation period started in late 2011 (Montgomery et al., 2015; Hill et al., 2020). Deformation source models have been produced by several authors for different uplift phases, using EDM, leveling, GNSS, InSAR and microgravity data. The most frequent solution, and preferred by the authors, is the one seeing the deformation source as a nearly vertical spheroidal shape, with a depth ranging from 6 to 10 km, located below the resurgent dome (Tiampo et al., 2000; Fialko et al., 2001; Battaglia et al., 2003; Langbein, 2003; Tizzani et al., 2009; Liu et al., 2011; Montgomery-Brown et al., 2015; Silverii et al., 2021). The mentioned studies implement the prolate spheroid source solution provided by Yang et al. (1988), except Langbein (2003), that used the moment tensor point-source described by Davis (1986). A vertical spheroidal cavity was also modeled using viscoelastic rheology by Newman et al. (2006). A review of the unrest at Long Valley is provided by Hill et al. (2020).

Although part of the observed deformation in Long Valley caldera has origin from hydrological processes, occurring at different spatial and temporal scales, and from seismic events (Silverii et al., 2020 and 2021), the main signals are proven to be related to deep dynamics of the caldera plumbing system. The involvement of magmatic, or of purely hydrothermal processes, at the origin of the observed signals is the object of an open scientific debate where geological and geophysical observations lead to contrasting conclusions (Hildreth, 2017; Hill, 2020). While geological studies support the non-magmatic unrest hypothesis, considering the caldera in a moribund stage (Hildreth, 2017), geophysics brings evidences of possible presence of partial melts in the mid- and lower crust, suggesting that the magmatic system is still active (Battaglia et al., 1999; Nakata and Shelly, 2018; Seccia et al., 2011).

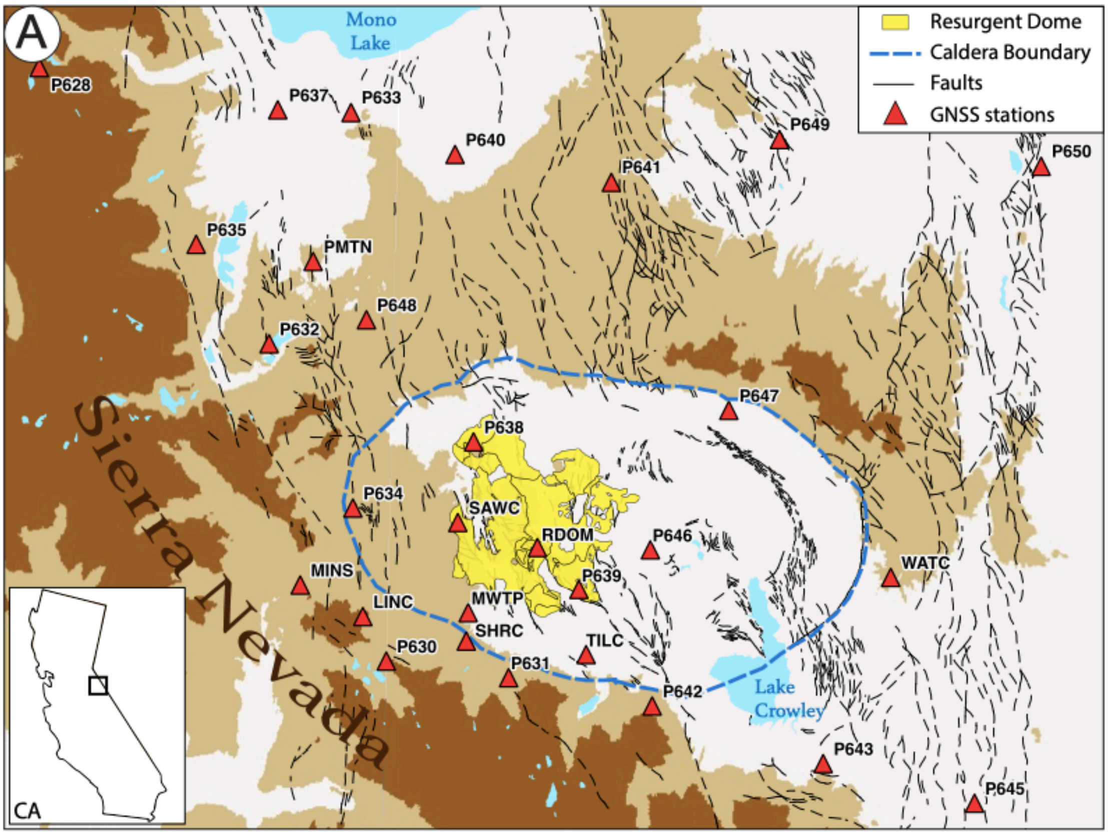

Figure 21. Simplified map of Long Valley caldera, CA, region. The map shows the caldera boundary (blue dotted line), the main structural lineaments (black lines), the area of the resurgent dome (yellow) and the locations of all the GNSS stations we used in this study.

5.2. Data

5.2.1. InSAR

We perform a multi-temporal InSAR analysis to map the ground deformation rates at the Long Valley caldera, adopting the Persistent Scatterers (PS) approach (Ferretti et al., 2001).

The PS technique (i.e., PS-InSAR, IPTA, STAMPS) analyzes only stable radar reflectors, consisting of single targets unaffected by temporal and spatial decorrelation, and we use a functional model of how deformation varies with time to identify PS pixels.

Acquisitions from multiple SAR missions are collected to detect the deformation field evolution through the years (Figure 2b, c, d). In particular, the analysis provided full temporal data coverage from the onset of the last inflation phase in late 2011 to late 2021 (Figure 22e). We collect images from ascending and descending orbits of SAR systems operating in the X- and C-band. In addition to the TerraSAR-X (TSX) descending orbit dataset from Montgomery et al. (2015), spanning the years 2011.3 - 2015.1, data from COSMO-SkyMed (CSK) and Sentinel-1 (S1) sensors has been processed. A total of 152 images have been considered in the analysis of CSK (125 for the ascending and 27 for the descending orbits, respectively). The ascending track data span the time from mid 2012 to 2017, while the descending from 2015 to mid 2016. The S1 dataset consists of 96 and 102 images (C-band, TOPSAR acquisition mode) for the ascending and descending orbits, respectively, covering the period from 2017 to 2020.

The SRTM Digital Elevation Model from the NASA Shuttle Mission (Farr et al., 2007) at 30 m ground resolution is used to remove the topographic contribution. The Goldstein filtering (Goldstein et al., 1988) is adopted to filter out the noise from all the interferometric pairs. Finally, the multi-temporal InSAR outcomes are geocoded in the WGS84 reference system. SAR data are processed using the Sarscape software (SARMAP®, CH).

The time series in Figure 22e compares the projected InSAR uplift velocities and the GNSS data at the RDOM station location. In this figure, we observe an inflation rate of slightly less than 2 cm/yr between 2011 and late 2014. Then, the inflation continues until 2021 but with a lower rate of a few mm/yr. The positive LOS signal since 2015 is retrieved by CSK descending orbit and S1 both orbits (Figure 22). To better exploit the different datasets and the corresponding temporal spans, we split the whole temporal interval in two main periods, T1 (from 2011 to end of 2014) and T2 (from January 2015 to end of 2021), according to Montgomery-Brown et al. (2015) and Silverii et al. (2021). In this way, we finally obtain two LOS velocity datasets, the first including TSX descending and CSK ascending, and the second dataset with ascending CSK and both orbits from S1. We exclude from the following analysis the descending CSK orbit data, since they are affected by high levels of noise, mainly due to the low number of available images preventing a reliable estimate and removal of the artifacts affecting data processing.

5.2.2. GNSS

Our dataset includes deformation velocities estimated from a dense network of GNSS continuous stations, distributed within the caldera and in the surroundings as shown in Figure 22a. The daily positions we use are available at https://earthquake.usgs.gov/monitoring/gps/LongValley (Murray and Svark, 2017). We start from NA-fixed trended time series and first remove the steady-state tectonic component, estimated for each station as the linear velocity rate in the time frame 2006-2010, a period of low deformation rates (Montgomery et al., 2015; Silverii et al., 2021). These velocities are obtained by means of a simple linear regression model. The study area is known to be affected by non-negligible deformation due to hydrological processes, as highlighted by Silverii et al. (2021), and by seismic swarms.

We, therefore, perform a correction of such signals, removing manually the semi-annual and annual oscillatory signals and the significant earthquake offsets using a GAMIT/GLOBK Matlab tool for time series analysis, *tsview* (http://www-gpsg.mit.edu/~tah/GGMatlab/). In particular, for the offset removal we consider the seismic catalog, available at https://earthquake.usgs.gov/earthquakes/search/, as a guide for a better interpretation. In this way, we filter most of the superimposed deformations, allowing for a more accurate estimate of the velocity rates associated to the caldera dynamics.

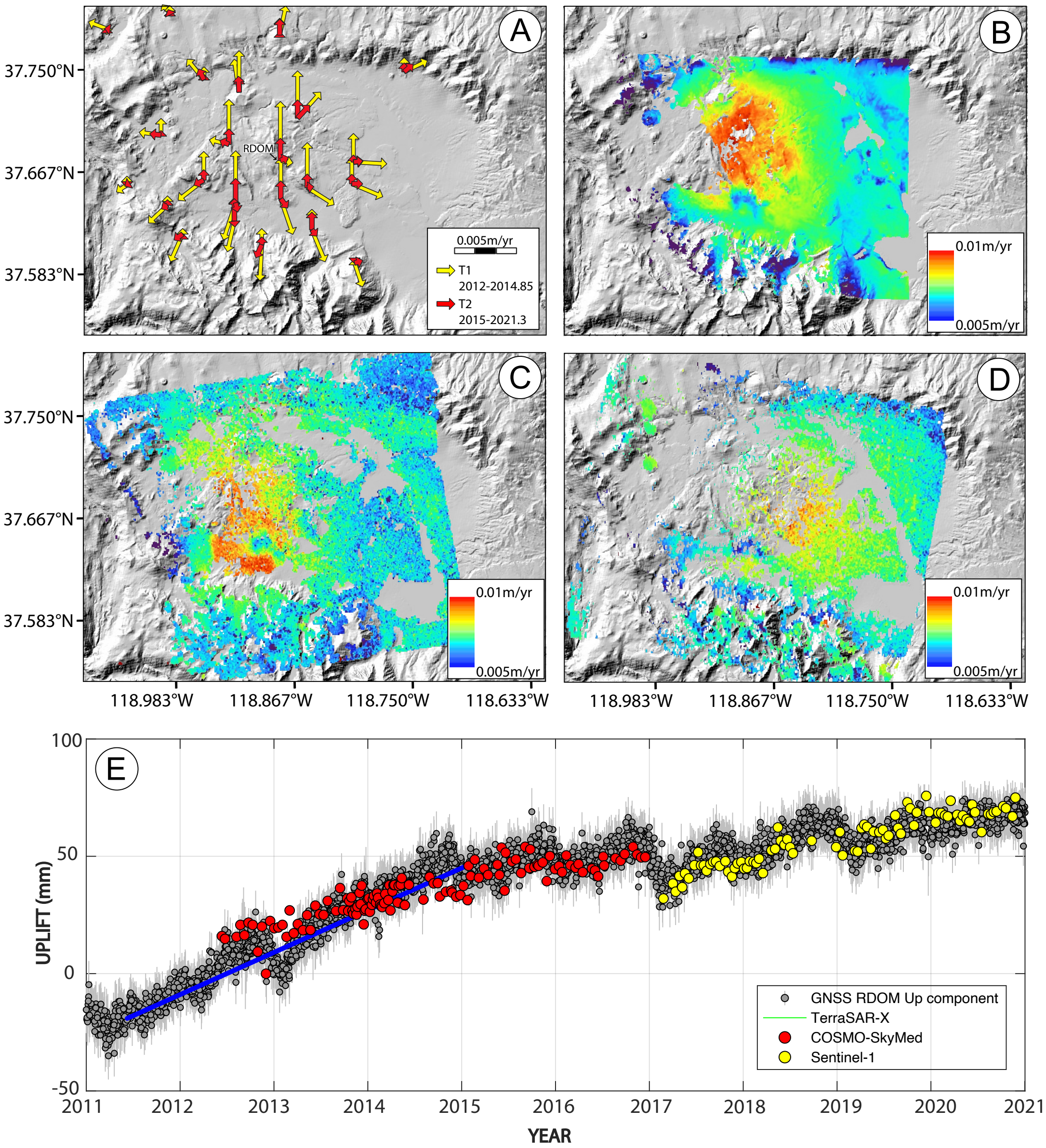

Figure 22. InSAR and GNSS data. a) GNSS velocities derived for T1 and T2 time intervals; b) InSAR COSMO-SkyMed ascending orbit data; c) InSAR Sentinel-1 ascending orbit data; d) InSAR Sentinel-1 descending data; e) Time series comparing the GNSS uplift velocity at RDOM station (grey) with InSAR decomposed up velocity components from TSX, CSK, S1 at the same location. The black dotted line marks the separation between T1 and T2.

For this task, we fit linear trends to the two temporal subsets of each time series, analogously to the approach employed for the InSAR data. The first phase, T1, spans the period from mid 2011 to end of 2014, while the second phase, T2, goes from January 2015 to mid 2021 (Figure 22e). We obtain velocities and errors for 36 stations selected for our models (Figure 22a). Finally, we consider the station P628 as a background velocity in the far field, assuming no deformation related to the caldera in that location. We remove this velocity from the whole dataset, to compensate possible inaccuracies in the removal of superimposed deformations due to non-volcanic processes.

5.3. Deformation source modeling of T1 and T2 phases.

We investigate the volcanic deformation source that caused the observed inflation within the caldera. The modeling software employed is the open-source Python tool VSM (Trasatti, 2022), using the Bayesian Inference algorithm implemented in this software as the sampling algorithm. We run separated inversions for the two periods suggested (T1, 2011-end of 2014 and T2, 2015- mid 2021) obtaining results for different model setups, setting different weights combinations among the data types, InSAR and GNSS. In this way, we investigate the influence of the type of dataset upon the model solution. We use subsampled InSAR datasets with higher density of points in the deformation area, discarding limited zones too noisy or affected by deformation of other nature. For example, in the subsiding area SW of the caldera a significant deformation is caused by the presence of geothermal power plants (Lagbein, 2003; Tizzani et al., 2007; Montgomery-Brown et al., 2015; Silverii et al., 2021), while in the South Moat (i.e. South Moat Seismic Zone, SMSZ) is due to the high rates of seismicity takes place. For further validation, we apply the same methodology to model the deformation source of a previous inflation phase observed in this area. We use leveling and EDM data (Battaglia et al., 2003), for the period spanning 1985-1999.

In this study, we use the moment tensor source described by Davis (1986) and implemented in VSM, for its versatility and the reduced number of parameters involved (see Introduction and Chapter 1). A limitation is the point-source approximation of the formulation, but it is suitable at Long Valley based on previous findings, since the source depth, between 6-10 km, is much larger than the source dimension (e.g., Battaglia et al., 2003; Newman et al., 2006; Montgomery-Brown et al., 2015).

Only a limited combination of moment tensor principal values can be interpreted in terms of triaxial ellipsoid (Trasatti et al., 2011). The shape (defined by the axes ratios) and the orientation (strike and dip) of the ellipsoid are determined based on the combination of the retrieved optimal dipoles and double couples. In particular, the source orientation is obtained by the eigenvectors from the diagonalization of the **Pij** matrix, while the relative size of the axes, b/a and c/a, where a is the maximum semi-axis, b is the intermediate and c is the minimum (a > b > c), are inversely related to the **Pij** eigenvalues (the moment tensor principal values $P_3 > P_2 > P_1$). The absolute axes size depends on the well known combination of VΔP/μ, where V is the source volume, ΔP the overpressure on the source boundary and μ is the shear modulus of the medium. Instead, we use Eq. 3 from Amoruso and Crescentini (2009) to estimate the volume change of the ellipsoidal inclusion, ΔV:

$$\Delta V = \frac{1-2\nu}{2(1+\nu)} \frac{P}{\mu} \left(\frac{P^T}{P} - 3 \right) \tag{10}$$

where, ν is the Posson’s ratio, P^T=P1+P2+P3. This formula points out that the volume variation depends on the ellipsoid shape, since it is determined from the ratios P_1 / P_3 and P_2 / P_3.

5.4. Results and discussions

From the analysis of the retrieved moment tensor values of the mean models sampled in the PPD distributions, we extract a series of parameters describing the sources. Knowing the principal moment tensor ratios, P_1 / P_3 and P_2 / P_3, we can infer the source geometry by plotting these values into the diagram represented in Figure 23a. All the solutions, for all the three periods we analyze, fall into the ellipsoids field. In particular, we find remarkably consistent parameters for the source shape, represented by a nearly vertical (averagely dipping with an angle of ~ 80°) ellipsoidal cavity, and with axis ratios b/a ~ 0.6 and c/a ~ 0.4 (Table 2, Figure23b, c).

These results persist among the different periods of interest, with independent datasets, and for changing data weights. For the two time phases T1 and T2 the source depth changes from ~ 7 km in T1 to ~ 5 km in T2. Also, the volume changes involved pass from $4.6\cdot10^6$ m^3/yr to $0.9\cdot10^6$ m^3/yr, consistently with the lower deformation velocities detected in the last years of the inflationary trend. In all the cases the source location falls in the area of the resurgent dome, but slightly migrates to the SE sector of the caldera in the T2 phase.

We compare these solutions with those obtained from the inversion of leveling and EDM data (Battaglia et al., 2003c) referred to the inflation of 1985-1999. Also in this case, we obtain a source with similar shape and orientation and a depth like the T1 source (~7 km). The volume change we estimate for this older event is 124 $\cdot10^6$ m^3, corresponding to a volume variation rate of ~ $8.86\cdot10^6$ m^3/yr. This volume variation estimate is nearly double the value we obtain for T1 (during 2011-2014), in accordance with the observed uplift rate in 1985-1999, twice the one we detect for T1 (respectively, 2.5 - 3.0 cm/yr against ~ 1.5 cm/yr). The PPD distributions of the model parameters and the model fit is presented in Supplementary Materials (Figures S2, S4, S5).

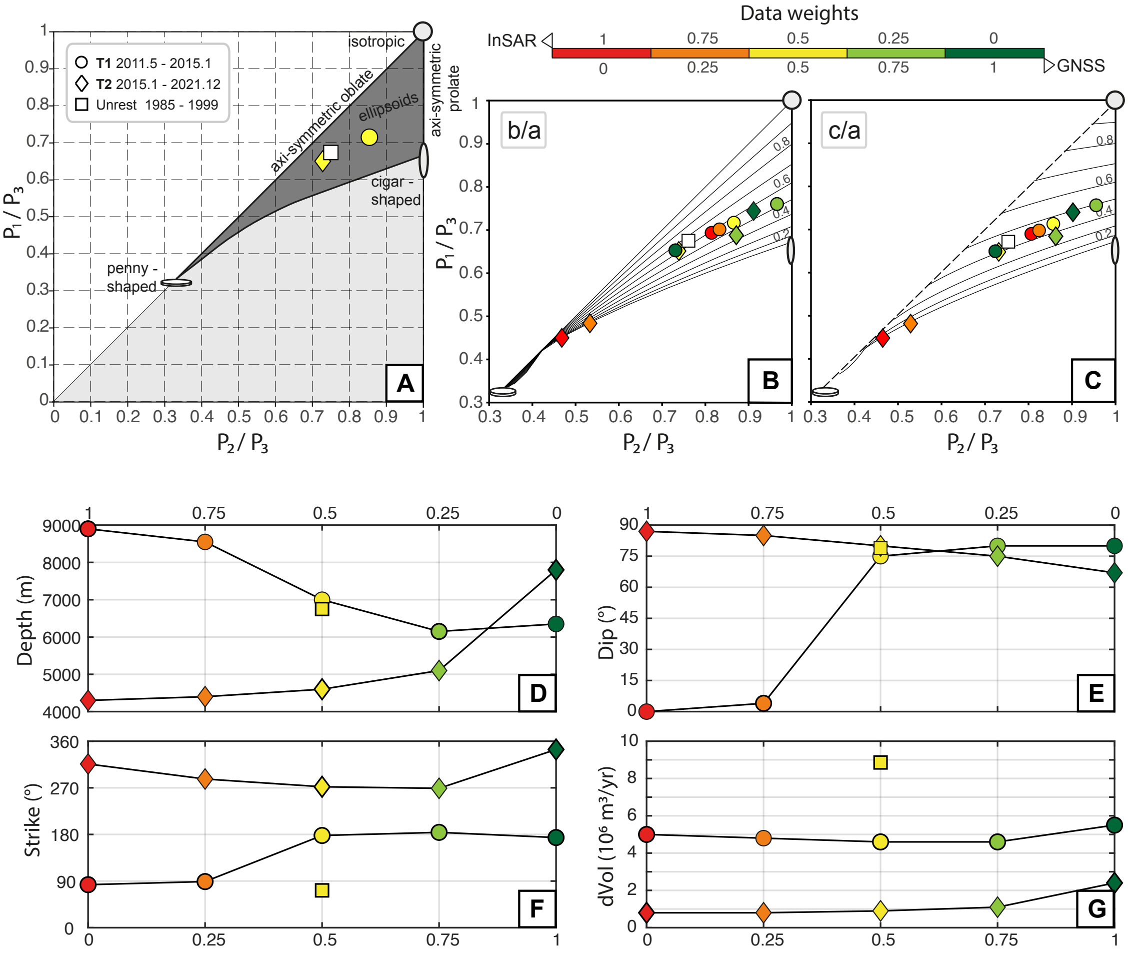

Figure 23. Results from the inversions for different unrest phases and different data types weight combinations. a) Principal moment tensor ratios defining the type of source geometry, the solutions fall in the ellipsoids field b,c) axis ratios based on the principal values ratios; the solutions lie along the b/a and c/a values of, respectively, ~0.6 and ~0.4; d) Depths for different data weight combinations e) Dip angles; f) Strike angles; g) Volume variations.

We observe that for the period T1 the GNSS data are well reproduced by the model (Figure S1a, b), except at MWTP station, which is located in the geothermal power plant area, where subsidence signals can be observed. The InSAR data from CSK ascending orbit are affected by significant noise (Figure S1c), therefore, residuals are considerably high in the western side of the caldera (Figure S1e). On the contrary, a good fit is shown for the TSX data, with residuals in the order of the data error

(Figure S1f, g, h). The same applies to T2 model fit, characterized by the highest residual for GNSS data near MWTP (Figure S3b), and in same area for the InSAR data, particularly in S1 ascending (Figure S3h). In general, also in this case the fit of the deformation field predicted by the model is satisfying, with residuals in the range of data uncertainties inside the caldera. Finally, we consider leveling and EDM data from the past unrest during 1985-1999. We apply the same methodology as for the recent data, and the results are shown in Figure S5. In this case, the comparison of observed and predicted data highlights a remarkably good fit of the leveling data, with very small residuals (Figure S5a, b, c). The EDM results are, as well, satisfyingly linearly correlated (Figure S5d)

Table 2. Mean parameters and associated errors from the inversion results for different unrest phases and different data types weight combinations.

InSAR weight	**GNSS weight**	**X UTM**	**Y UTM**	**depth (m)**	**dip (°)**	**strike (°)**	**s.rot (°)**	**b/a**	**c/a**	**P2/P3**	**P1/P3**	**dVol/yr (10^6 m3/yr)**
T1												
1	**0**	329050 ±50	4173400 ±100	8900±150	-2	83	-6	0,72	0,28	0,4634	0,4487	5 ±0,086
0,75	**0,25**	329400 ±100	4173100 ±150	8550±100	4	89	-3	0,33	0,16	0,5277	0,4820	4,8 ±0,088
0,5	**0,5**	330200 ±100	4173100 ±100	7000±100	75	178	-3	0,62	0,40	0,7313	0,6475	4,6 ±0,075
0,25	**0,75**	330650 ±50	4172950 ±100	6150±100	80	184	2	0,44	0,36	0,8629	0,6836	4,6 ±0,088
0	**1**	330950 ±100	4172750 ±100	6350±150	80	174	73	0,51	0,45	0,9026	0,7235	5,5 ±0,147
T2												
1	**0**	333300 ±100	4172100 ±200	4300±200	87	316	-19	0,59	0,44	0,8064	0,6891	0,8 ±0,033
0,75	**0,25**	333200 ±100	4172000 ±200	4400±200	85	287	-19	0,58	0,44	0,8244	0,6970	0,8 ±0,032
0,5	**0,5**	333000 ±150	4171700 ±250	4600±200	80	272	-20	0,56	0,46	0,8573	0,7122	0,9 ±0,041
0,25	**0,75**	332450 ±150	4171200 ±250	5100±250	75	269	-25	0,52	0,49	0,9562	0,7551	1,1 ±0,058
0	**1**	330200 ±300	4170750 ±250	7800±400	67	344	70	0,60	0,40	0,7390	0,6490	2,4 ±0,58
Unrest 85-99												
Leveling weight	**EDM weight**											
0,5	**0,5**	331800±150	4172900 ±150	6750±200	79	72	-64	0,66	0,44	0,7530	0,6710	8.86 ± 5,420

5.5. Conclusion

The outcomes of this study highlight that the deformation of Long Valley caldera can be explained by the presence of a pressurized source at depth. Our models are supported by an extensive dataset, with multi-satellite InSAR data and GNSS, that reinforcing the reliability of our results. The misfit in our models is mostly located in the area of the geothermal power plants, near GNSS station MWTP, similarly to what results from the analysis of Montgomery et al. (2015). Also, we observe in the InSAR data deformations that cannot be resolved by the source model, along the western side of the caldera. We attribute the associated deformation signals as a superimposed deformation due to the hydrological processes acting in the area of the Mammoth Lakes, in accord with the findings of Silverii et al. (2020,2021). In fact, no corrections for the non-negligible superimposed deformation signals can be applied to InSAR, contrarily to what we did for GNSS velocities (see section 5.2.2.).

The deformation source, according to our findings, has an ellipsoidal shape, vertically oriented. The retrieved parameters describing the source shape are consistent in all the three periods we analyzed with independent datasets. Also, our results are consistent with the deformation source models presented in the literature. A key point deriving from our analysis is that the source depth remained mostly stable to ~ 7 km from the 1985-99 unrest to 2015, end of the phase T1 according to our distinction. From 2015, we retrieve a source at shallower depth (~ 5 km) suggesting the possibility of some intrusive process ascent. However, in the second phase of the last unrest, the source location slightly changes, moving towards the South Eastern sector of the caldera.

Conclusions and future developments

In this thesis, we presented an original deformation source modeling approach based on Finite Element Methods. We develop a specific trans-dimensional algorithm to deal with our problem, that sees the deformation source shaped in a FE-mesh free of cavities and a-priori geometric constraints. The aim is to represent more realistic pressurized magma reservoirs in comparison with the solutions proposed by the existing methods, avoiding the user control on the source geometry and letting the solution be purely guided by the data.

Differently from previous attempts in the literature, using Finite Elements Methods to model free shaped sources, this method solves the point-source limitation we discussed in the Introduction of this thesis. We create, in fact, an original forward model that is used as the elementary unit of a composite source assembly, with features that allow to rigorously account for fundamental continuum mechanics principles, as we prove by means of several synthetic tests. This unit is obtained by loading solid cubic elements of the FE grid with a unitary stress tensor. We apply the six stress tensor components, normal and shear, in the form of dipoles and double couples of forces acting on each element faces using a FEM commercial software (i.e. Marc Mentat 2013). The six surface displacements, relative to each stress component applied, are computed for each unit in a given source assembly. This deformation can be summed and linearly scaled to obtain the total deformation field according to the superposition principle. We verify with synthetic tests the equivalence of the deformation fields caused by pressurized cavities with uniform pressure applied at their boundaries and that caused by our assembly with scaled stress components.

Also, our method represents a cost-efficient approach permitting to avoid computationally expensive re-meshing processes, as our forward model is built in a continuum domain without cavities. Therefore, we exploit the possibility to pre-compute unitary displacements on a fixed mesh, that can be stored and combined a-posteriori for our simulations.

We develop an inversion code handling the information in the matrix of pre-computed unitary responses and producing models of the deformation source based on geodetic datasets of different types. The code is characterized by a high level of sophistication, employing Bayesian inference and the reversible-jump McMC (Trans-D) approach, that deals with numerical problems of changing dimensions. The number of parameters is inverted itself and consists of the number of partitions of the three-dimensional model space that are required to shape the deformation source. In particular, we use a Voronoi diagram made of two competing sets of polyhedral three-dimensional Voronoi cells that sample the domain and define the volume occupied by the deformation source. The use of two trans-dimensional elements (i.e. two sets of cells) represents a novel application in Trans-D algorithms.

We highlight the potential of our code with synthetic tests and future applications to real case studies are planned, as well as code improvements for ever more efficiency. In fact, the complexity of the problem and the variety of analysis options we foresee requires more work and investigation about the logic of the algorithm. One of the short-term goals is the introduction of parallelization options (i.e. master/slave CPUs) for a more efficient chain sampling and shorter computational time; therefore, a higher number of data points allowed. We aim, then, to the real case study application at the Long Valley caldera volcanic site, the subject of our preparatory study presented in Chapter 5.

Finally, the proposed approach represents a promising starting point for the retrieval of fully irregular sources with inverse modeling, one of the main targets in the volcanic deformation source modeling field now that large datasets with unprecedented accuracy are accessible.

References

Acocella, V. (2019). Bridging the gap from caldera unrest to resurgence. *Frontiers in Earth Science*, *7*, 173.

Amoruso, A., & Crescentini, L. (2009). Shape and volume change of pressurized ellipsoidal cavities from deformation and seismic data. *Journal of Geophysical Research: Solid Earth*, *114*(B2). doi:10.1029/2008JB005946.

Amoruso, A., & Crescentini, L. (2013). Analytical models of volcanic ellipsoidal expansion sources. *Annals of Geophysics*, *56*(4), S0435-S0435. doi:10.4401/ag-6441.

Bagnardi, M., and Hooper, A. (2018). Inversion of Surface Deformation Data for Rapid Estimates of Source Parameters and Uncertainties: A Bayesian Approach. Geochem. Geophys. Geosyst. 19, 2194–2211. doi:10.1029/2018GC007585

Battaglia, M., Roberts, C., & Segall, P. (1999). Magma intrusion beneath Long Valley caldera confirmed by temporal changes in gravity. *Science*, *285*(5436), 2119-2122.

Battaglia, M., Segall, P., & Roberts, C. (2003). The mechanics of unrest at Long Valley caldera, California. 2. Constraining the nature of the source using geodetic and micro-gravity data. *Journal of Volcanology and Geothermal Research*, *127*(3-4), 219-245. doi: 10.1016/S0377-0273(03)00171-9.

Battaglia, M., Cervelli, P. F., and Murray, J. R. (2013). Modeling Crustal Deformation Near Active Faults and Volcanic Centers—A Catalog of Deformation Models. Available at: http://pubs.er.usgs.gov/publication/tm13B1.

Bayes, T. (1763). LII. An essay towards solving a problem in the doctrine of chances. By the late Rev. Mr. Bayes, FRS communicated by Mr. Price, in a letter to John Canton, AMFR S. *Philosophical transactions of the Royal Society of London*, (53), 370-418.

Biggs, J., Ebmeier, S. K., Aspinall, W. P., Lu, Z., Pritchard, M. E., Sparks, R. S. J., & Mather, T. A. (2014). Global link between deformation and volcanic eruption quantified by satellite imagery. *Nature communications*, *5*(1), 1-7.

Biggs, J., and Wright, T. J. (2020). How Satellite InSAR Has Grown from Opportunistic Science to Routine Monitoring over the Last Decade. Nat. Commun. 11, 3863. doi:10.1038/s41467-020-17587-6

Bodin, T., & Sambridge, M. (2009). Seismic tomography with the reversible jump algorithm. *Geophysical Journal International*, *178*(3), 1411-1436.

Burchardt S. , Tanner D.C., Krumbholz M., 2010. Mode of emplacement of the Slaufrudalur Pluton, Southeast Iceland inferred from three-dimensional GPS mapping and model building, *Tectonophysics*480(1–4), 232–240.

Camacho, A. G., González, P. J., Fernández, J., & Berrino, G. (2011). Simultaneous inversion of surface deformation and gravity changes by means of extended bodies with a free geometry: Application to deforming calderas. *Journal of Geophysical Research: Solid Earth*, *116*(B10).

Casu, F., Manzo, M., & Lanari, R. (2006). A quantitative assessment of the SBAS algorithm performance for surface deformation retrieval from DInSAR data. *Remote Sensing of Environment*, *102*(3-4), 195-210.

Davis, P. M. (1986). Surface Deformation Due to Inflation of an Arbitrarily Oriented Triaxial Ellipsoidal Cavity in an Elastic Half-Space, with Reference to Kilauea Volcano, Hawaii. J. Geophys. Res. 91, 7429–7438. doi:10.1029/ jb091ib07p07429

Denison, D. G., Holmes, C. C., Mallick, B. K., & Smith, A. F. (2002). *Bayesian methods for nonlinear classification and regression* (Vol. 386). John Wiley & Sons.

Dzurisin, D. (2003). A comprehensive approach to monitoring volcano deformation as a window on the eruption cycle. *Reviews of Geophysics*, *41*(1).

Eshelby, J. D. (1957). The Determination of the Elastic Field of an Ellipsoidal Inclusion, and Related Problems. Proc. R. Soc. Lond. A 241, 376–396. doi:10.1098/ rspa.1957.0133

Farr, T. G., et al. (2007), The Shuttle Radar Topography Mission, Rev. Geophys., 45, RG2004, doi:10.1029/2005RG000183.

Ferrari, C., Bonafede, M., & Trasatti, E. (2015). Relations between pressurized triaxial cavities and moment tensor distributions. *Annals of Geophysics*, *58*(4), S0438-S0438.

Ferretti A., Prati C. and Rocca F.; 2001: Permanent scatterers in SAR interferometry. IEEE Trans. Geosci. Remote Sens., 39, 8-20.

Fialko, Y., Khazan, Y., and Simons, M. (2001). Deformation Due to a Pressurized Horizontal Circular Crack in an Elastic Half-Space, with Applications to Volcano Geodesy. Geophys. J. Int. 146, 181–190. doi:10.1046/j.1365-246X.2001.00452.x

Geyer, C.J. & Møller, J., 1994. Simulation procedures and likelihood infer- ence for spatial point processes, Scand. J. Stats., 21, 359–373.

Gelman, A., Roberts, G.O. & Gilks, W.R., 1996. Efficient Metropolis Jumping Rules, Oxford University Press, 599–607 pp

Goldstein R.M., Zebker H.A. and Werner C.L.; 1988: Satellite radar interferometry: two-dimensional phase unwrapping. Radio Sci., 23, 713-720.

Green, P. J. (1995). Reversible jump Markov chain Monte Carlo computation and Bayesian model determination. *Biometrika*, *82*(4), 711-732.

Hastings, W.K., 1970. Monte Carlo sampling methods using Markov chains and their applications, Biometrica, 57, 97–109.

Hawkins, R., Bodin, T., Sambridge, M., Choblet, G., & Husson, L. (2019). Trans-dimensional surface reconstruction with different classes of parameterization. *Geochemistry, Geophysics, Geosystems*, *20*(1), 505-529.

Hickey, J., Gottsmann, J., & Mothes, P. (2015). Estimating volcanic deformation source parameters with a finite element inversion: The 2001–2002 unrest at Cotopaxi volcano, Ecuador. *Journal of Geophysical Research: Solid Earth*, *120*(3), 1473-1486.

Hill, D. P., Montgomery-Brown, E. K., Shelly, D. R., Flinders, A. F., & Prejean, S. (2020). Post-1978 tumescence at Long Valley caldera, California: A geophysical perspective. *Journal of Volcanology and Geothermal Research*, *400*, 106900.

Hildreth, W. (2017). Fluid-driven uplift at Long Valley Caldera, California: geologic perspectives. *Journal of Volcanology and Geothermal Research*, *341*, 269-286.

Huang H.H. , Lin F.C., Schmandt B., Farrell J., Smith R.B., Tsai V.C., 2015. The Yellowstone magmatic system from the mantle plume to the upper crust, *Science*348, doi:10.1126/science.aaa5648.

Langbein, J. O. (2003). Deformation of the Long Valley Caldera, California: inferences from measurements from 1988 to 2001. *Journal of Volcanology and Geothermal Research*, *127*(3-4), 247-267.

Lisowski, M. (2007). Analytical volcano deformation source models. In *Volcano deformation* (pp. 279-304). Springer, Berlin, Heidelberg.

Liu, Z., Dong, D., Lundgren, P., 2011. Constraints on time-dependent volcanic source models at Long Valley Caldera from 1996 to 2009 using InSAR and geodetic measure- ments. Geophys. J. Int. 187 (3), 1283–1300.

Malinverno, A. (2002). Parsimonious Bayesian Markov chain Monte Carlo inversion in a nonlinear geophysical problem. *Geophysical Journal International*, *151*(3), 675-688.

Malinverno, A., & Briggs, V. A. (2004). Expanded uncertainty quantification in inverse problems: Hierarchical Bayes and empirical Bayes. *Geophysics*, *69*(4), 1005-1016.

Mandolesi, E., Ogaya, X., Campanyà, J., & Agostinetti, N. P. (2018). A reversible-jump Markov chain Monte Carlo algorithm for 1D inversion of magnetotelluric data. *Computers & Geosciences*, *113*, 94-105.

Masterlark T. , Lu Z., 2004. Transient volcano deformation sources imaged with interferometric synthetic aperture radar: application to Seguam Island, Alaska, *J. geophys. Res.*109, B01401, doi:10.1029/2003JB002568.

McTigue, D. F. (1987). Elastic Stress and Deformation Near a Finite Spherical Magma Body: Resolution of the Point Source Paradox. J. Geophys. Res. 92, 12931. doi:10.1029/jb092ib12p12931

Metropolis, N., Rosenbluth, A. W., Rosenbluth, M. N., Teller, A. H., & Teller, E. (1953). Equation of state calculations by fast computing machines. *The journal of chemical physics*, *21*(6), 1087-1092.Mogi, K. (1958). Relations between the Eruptions of Various Volcanoes and the Deformations of the Ground Surfaces Around Them. Bull. Earthq. Res. Inst. 36, 99– 134.

Montgomery-Brown, E. K., Wicks, C. W., Cervelli, P. F., Langbein, J. O., Svarc, J. L., Shelly, D. R., Hill, D.P. & Lisowski, M. (2015). Renewed inflation of long valley caldera, california (2011 to 2014). *Geophysical Research Letters*, *42*(13), 5250-5257. doi: 10.1002/2015GL064338.

Mosegaard, K., 2006. Monte Carlo analysis of inverse problem, PhD thesis, Copenhagen University.

Mosegaard, K., & Tarantola, A. (1995). Monte Carlo sampling of solutions to inverse problems. *Journal of Geophysical Research: Solid Earth*, *100*(B7), 12431-12447.

Mossop, A., & Segall, P. (1999). Volume strain within The Geysers geothermal field. *Journal of Geophysical Research: Solid Earth*, *104*(B12), 29113-29131.

Murray, J. R., & Svarc, J. (2017). Global Positioning System data collection, processing, and analysis conducted by the US Geological Survey Earthquake Hazards Program. *Seismological Research Letters*, *88*(3), 916-925. doi: 10.1785/0220160204.

Newhall, C. G., & Dzurisin, D. (1988). *Historical unrest at the large calderas of the world* (No. 1855). Department of the Interior, US Geological Survey.

Newman, A.V., Dixon, T.H., Gourmelen, N., 2006. A four-dimensional viscoelastic de- formation model for Long Valley Caldera, California, between 1995 and 2000. J. Volcanol. Geotherm. Res. 150 (1–3), 244–269. https://doi.org/10.1016/j.jvolgeores.2005.07.017.

Okada, Y. (1985). Surface Deformation Due to Shear and Tensile Faults in a Half-Space. Int. J. Rock Mech. Min. Sci. Geomech. Abstr. 75, 1135–1154. doi:10.1785/bssa0750041135.

Piana Agostinetti, N., Giacomuzzi, G., & Malinverno, A. (2015). Local three-dimensional earthquake tomography by trans-dimensional Monte Carlo sampling. *Geophysical Journal International*, *201*(3), 1598-1617.

Piana Agostinetti, N., & Sgattoni, G. (2021). Changepoint detection in seismic double-difference data: application of a trans-dimensional algorithm to data-space exploration. *Solid Earth*, *12*(12), 2717-2733.

Poland, M. P., and de Zeeuw-van Dalfsen, E. (2021). “Volcano Geodesy: A Critical Tool for Assessing the State of Volcanoes and Their Potential for Hazardous Eruptive Activity,” in Forecasting and Planning for Volcanic Hazards, Risks, and Disasters (Amsterdam, Netherlands: Elsevier), 75–115. doi:10.1016/b978-0-12-818082-2.00003-2

Robič, T., & Filipič, B. (2005). Differential evolution for multiobjective optimization. In Evolutionary Multi-Criterion Optimization: Third International Conference, EMO 2005, Guanajuato, Mexico, March 9-11, 2005. Proceedings 3 (pp. 520-533). Springer Berlin Heidelberg.

Ronchin, E., Masterlark, T., Dawson, J., Saunders, S., & Martì Molist, J. (2017). Imaging the complex geometry of a magma reservoir using FEM-based linear inverse modeling of InSAR data: application to Rabaul Caldera, Papua New Guinea. *Geophysical Journal International*, *209*(3), 1746-1760.

Rosi, M., Acocella, V., Cioni, R., Bianco, F., Costa, A., De Martino, P., ... & Inguaggiato, S. (2022). Defining the pre-eruptive states of active volcanoes for improving eruption forecasting. *Frontiers in Earth Science*.

Sambridge, M., Braun, J., & McQueen, H. (1995). Geophysical parametrization and interpolation of irregular data using natural neighbours. *Geophysical Journal International*, *122*(3), 837-857.

Sambridge, M., & Faletič, R. (2003). Adaptive whole Earth tomography. *Geochemistry, Geophysics, Geosystems*, *4*(3).

Sambridge, M., & Mosegaard, K. (2002). Monte Carlo methods in geophysical inverse problems. *Reviews of Geophysics*, *40*(3), 3-1.

Seccia, D., Chiarabba, C., De Gori, P., Bianchi, I., Hill, D.P., 2011. Evidence for the contempo- rary magmatic system beneath Long Valley Caldera from local earthquake tomogra- phy and receiver function analysis. J. Geophys. Res. 116 (B12). https://doi.org/ 10.1029/2011JB008471.

Segall, P. (2010). Earthquake and Volcano Deformation. New Jersey, United States: Princeton Univeristy Press. doi:10.1515/9781400833856.

Nakata, N., Shelly, D.R., 2018. Imaging a crustal low-velocity layer using reflected seismic waves from the 2014 Earthquake Swarm at Long Valley Caldera, California: the Mag- matic System Roof? Roof of magmatic system at long valley. Geophys. Res. Lett. 45 (8), 3481–3488. https://doi.org/10.1029/2018GL077260.

Silverii, F., Montgomery-Brown, E. K., Borsa, A. A., & Barbour, A. J. (2020). Hydrologically induced deformation in long valley caldera and adjacent Sierra Nevada. *Journal of Geophysical Research: Solid Earth*, *125*(5), e2020JB019495.

Silverii, F., Pulvirenti, F., Montgomery-Brown, E. K., Borsa, A. A., & Neely, W. R. (2021). The 2011-2019 Long Valley Caldera inflation: New insights from separation of superimposed geodetic signals and 3D modeling. *Earth and Planetary Science Letters*, *569*, 117055. doi: 10.1016/j.epsl.2021.117055 .

Smith R.B. et al. , 2009. Geodynamics of the Yellowstone hotspot and mantle plume: seismic and GPS imaging, kinematics, and mantle flow, *J. Volc. Geotherm. Res.*188(1–3), 26–56

Tarantola, A. (2006). Popper, Bayes and the inverse problem. *Nature physics*, *2*(8), 492-494.

Tiampo, K.F., Rundle, J.B., Fernandez, J., Langbein, J.O., 2000. Spherical and ellipsoidal vol- canic sources at Long Valley caldera, California, using a genetic algorithm inversion technique. J. Volcanol. Geotherm. Res. 102 (3–4), 189–206. https://doi.org/10.1016/ S0377-0273(00)00185-2.

Tizzani, P., Berardino, P., Casu, F., Euillades, P., Manzo, M., Ricciardi, G. P., ... & Lanari, R. (2007). Surface deformation of Long Valley caldera and Mono Basin, California, investigated with the SBAS-InSAR approach. *Remote Sensing of Environment*, *108*(3), 277-289.

Trasatti, E. (2022). Volcanic and seismic source modeling: an open tool for geodetic data modeling. *Frontiers in Earth Science*.

Trasatti, E., Bonafede, M., Ferrari, C., Giunchi, C., and Berrino, G. (2011). On Deformation Sources in Volcanic Areas: Modeling the Campi Flegrei (Italy) 1982-84 Unrest. Earth Planet. Sci. Lett. 306, 175–185. doi:10.1016/j.epsl.2011.03.033

Trasatti, E., Giunchi, C., & Bonafede, M. (2003). Effects of topography and rheological layering on ground deformation in volcanic regions. *Journal of Volcanology and Geothermal Research*, *122*(1-2), 89-110.

Trasatti, E., Giunchi, C., & Agostinetti, N. P. (2008). Numerical inversion of deformation caused by pressure sources: application to Mount Etna (Italy). *Geophysical Journal International*, *172*(2), 873-884.

Vasco, D. W., Wicks Jr, C., Karasaki, K., & Marques, O. (2002). Geodetic imaging: reservoir monitoring using satellite interferometry. *Geophysical Journal International*, *149*(3), 555-571.

Yang, X.-M., Davis, P. M., and Dieterich, J. H. (1988). Deformation from Inflation of a Dipping Finite Prolate Spheroid in an Elastic Half-Space as a Model for Volcanic Stressing. J. Geophys. Res. 93, 4249–4257. doi:10.1029/ JB093iB05p04249

Supplementary materials

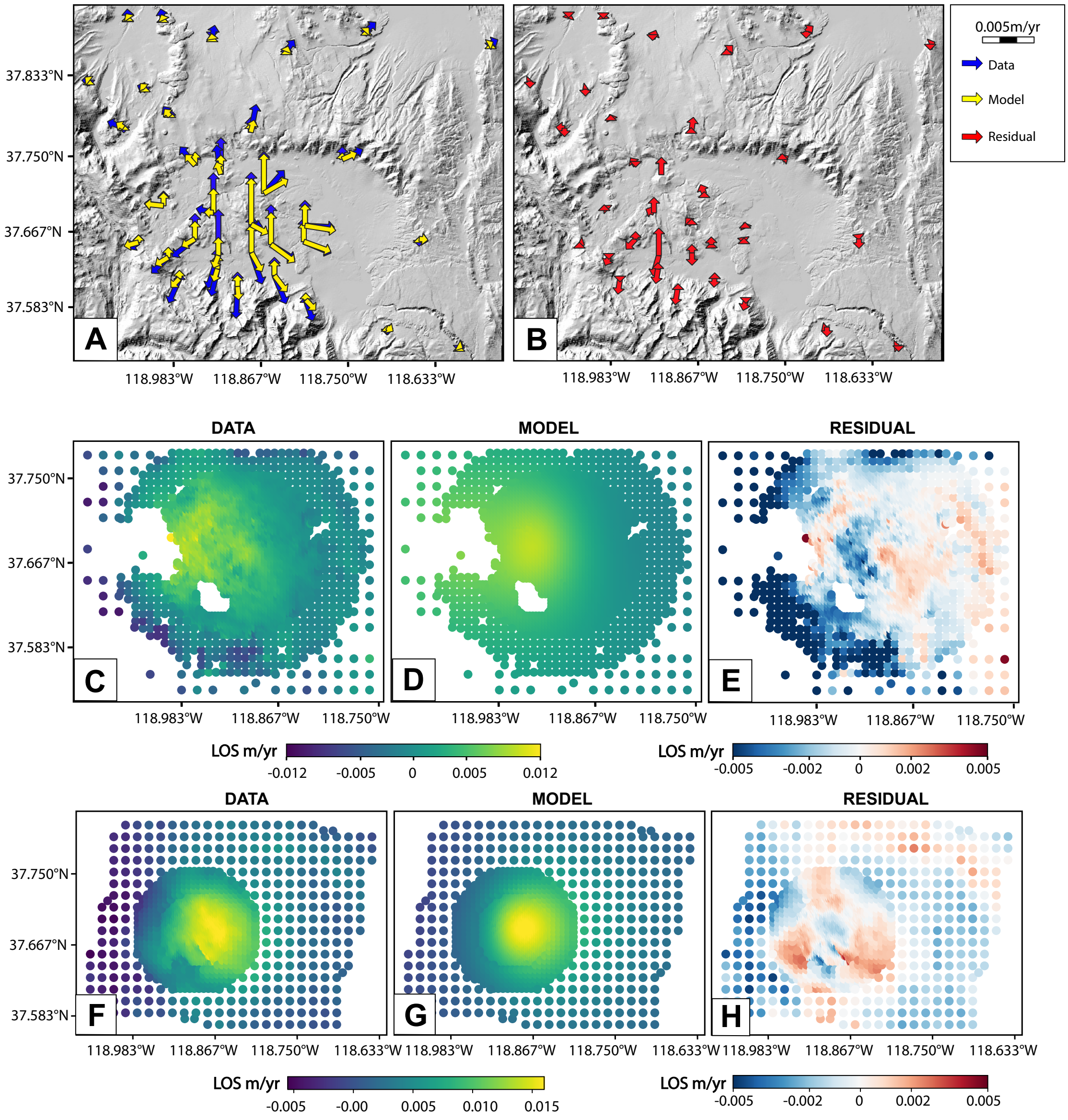

Figure S1. Model fit for the phase T1 relative to the inversion with data weight Insar 0,5 and GNSS 0,5. a) Comparison between observed and predicted GNSS velocities; b) GNSS residuals; c,d,e) Data, Model, Residual of COSMO-SkyMed InSAR data; f,g,h) Data, Model, Residual of TerraSAR-X data.

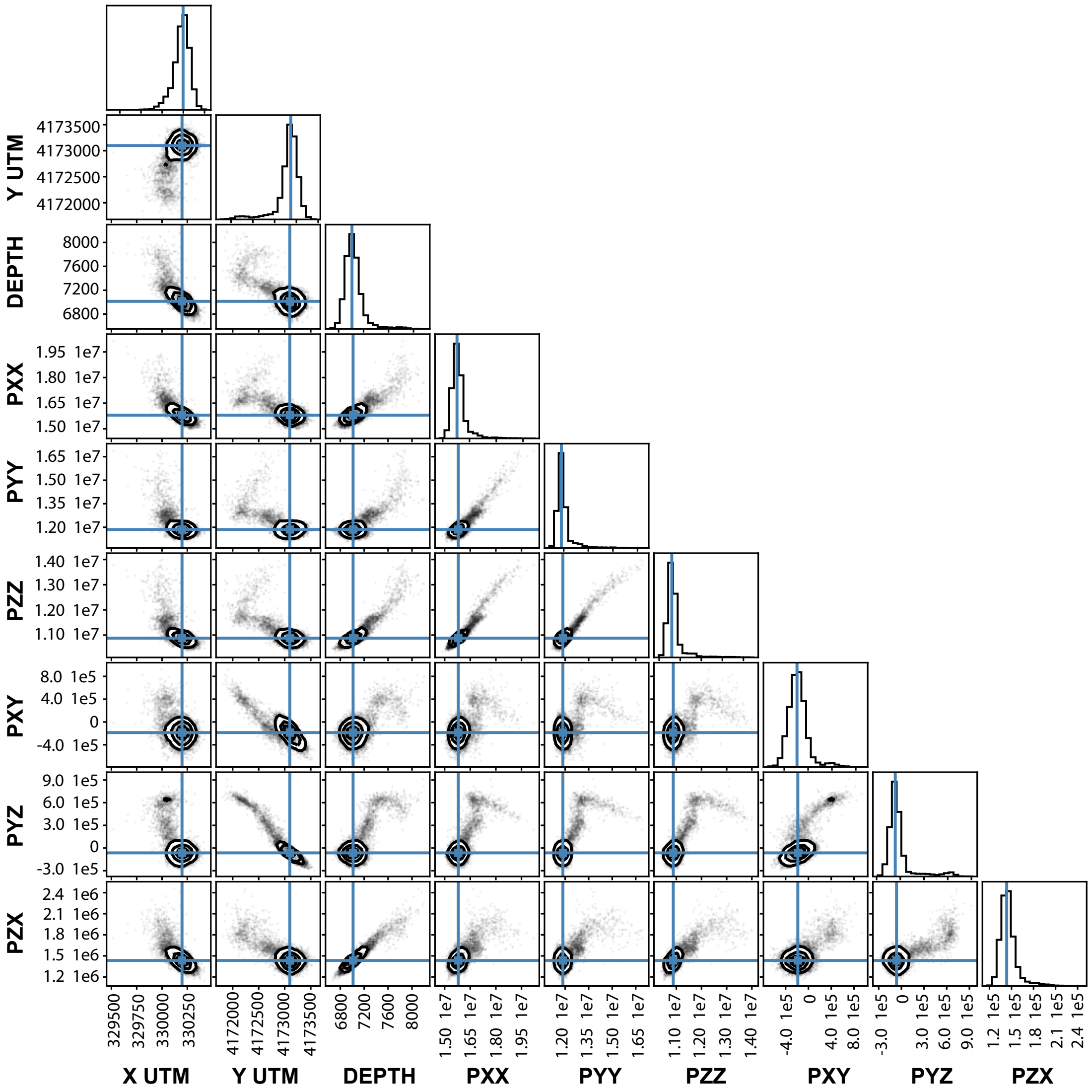

Figure S2. Parameters distributions for the inversion of the T1 dataset.

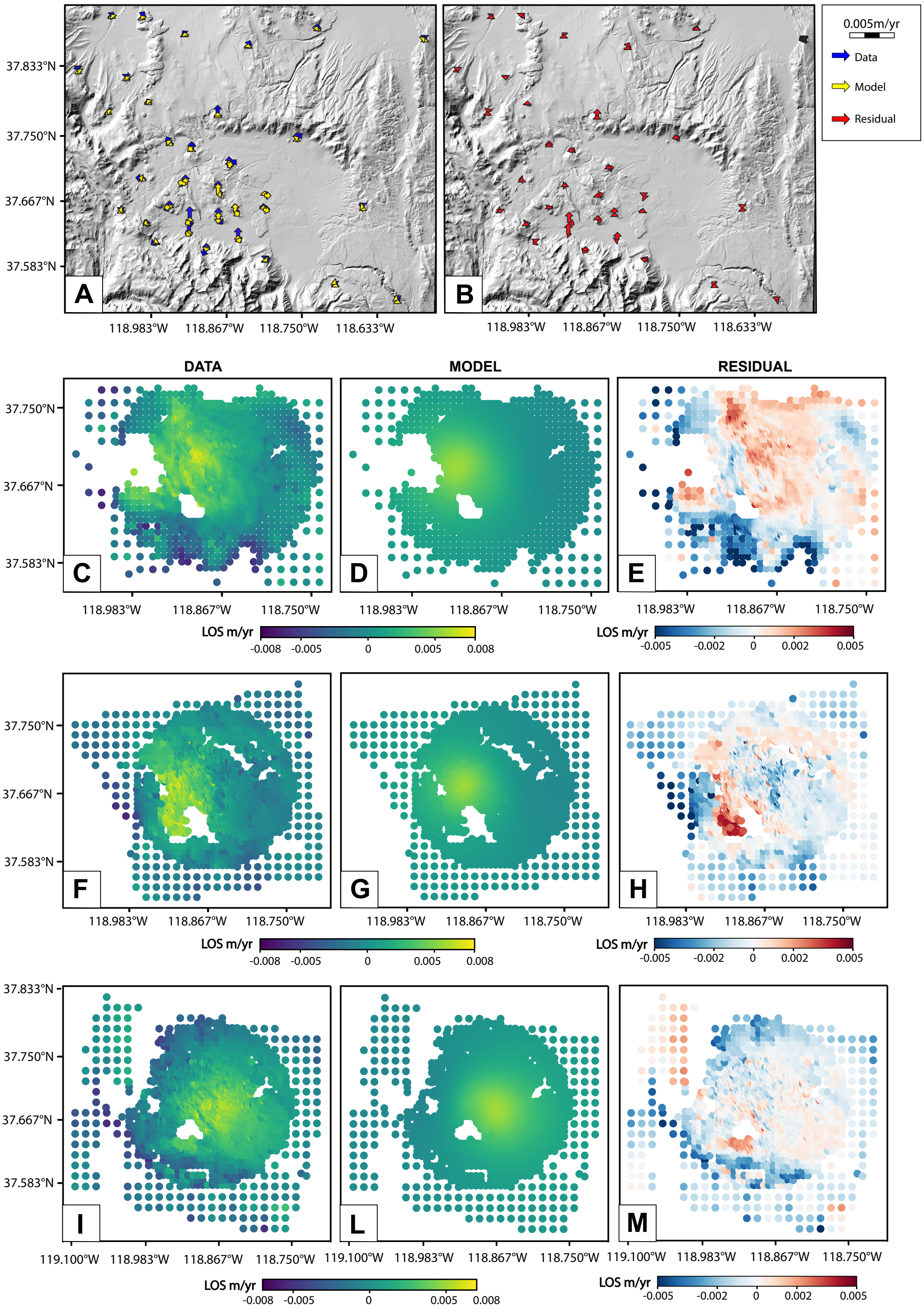

Figure S3. Model fit for the phase T2 relative to the inversion with data weight Insar 0,5 and GNSS 0,5. a) Comparison between observed and predicted GNSS velocities; b) GNSS residuals; c,d,e) Data, Model, Residual of COSMO-SkyMed InSAR data; f,g,h) Data, Model, Residual of Sentinel-1 ascending data; i,l,m) Data, Model, Residual of Sentinel-1 descending data.

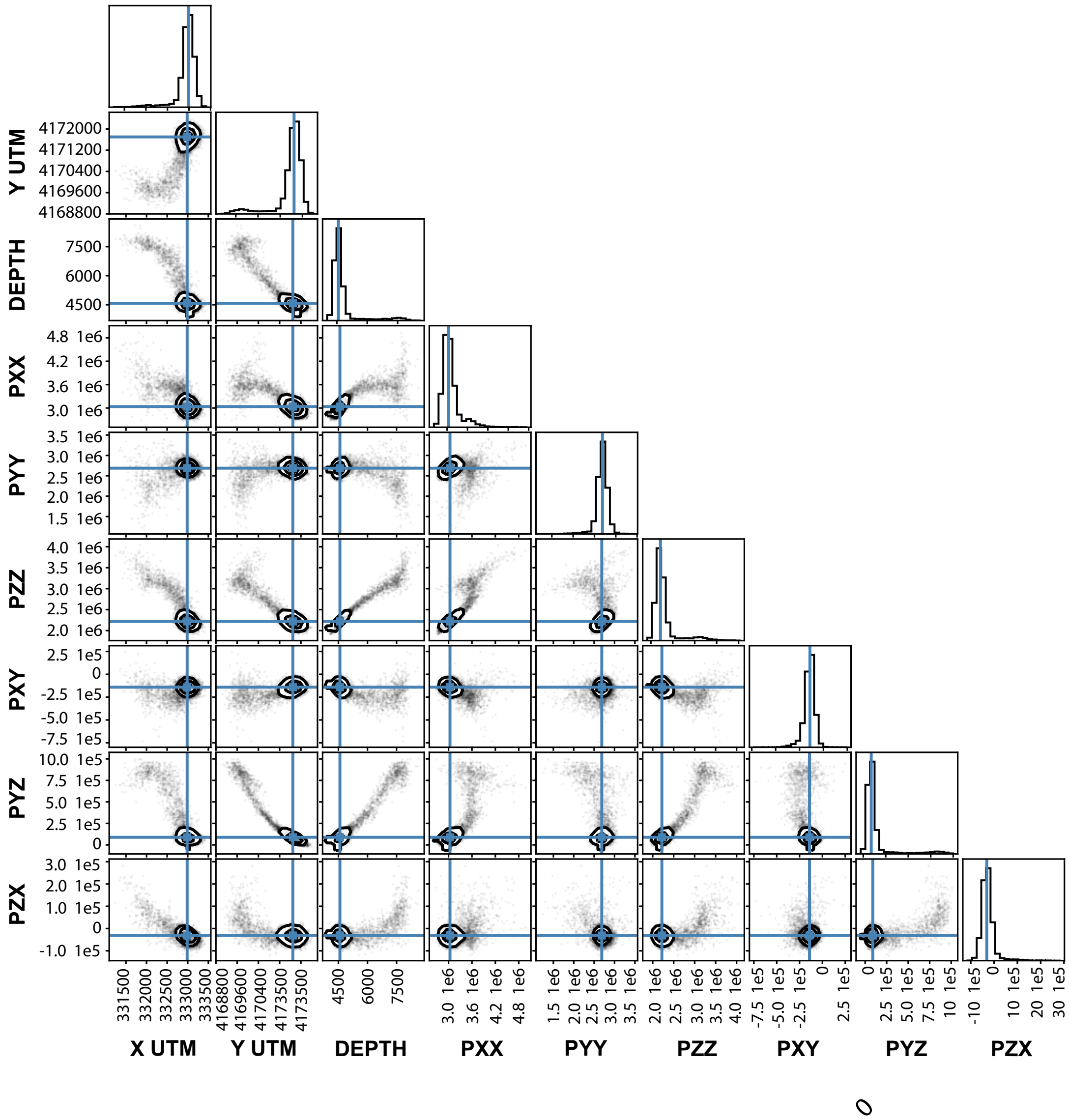

Figure S4. Parameters distributions for the inversion of the T2 dataset

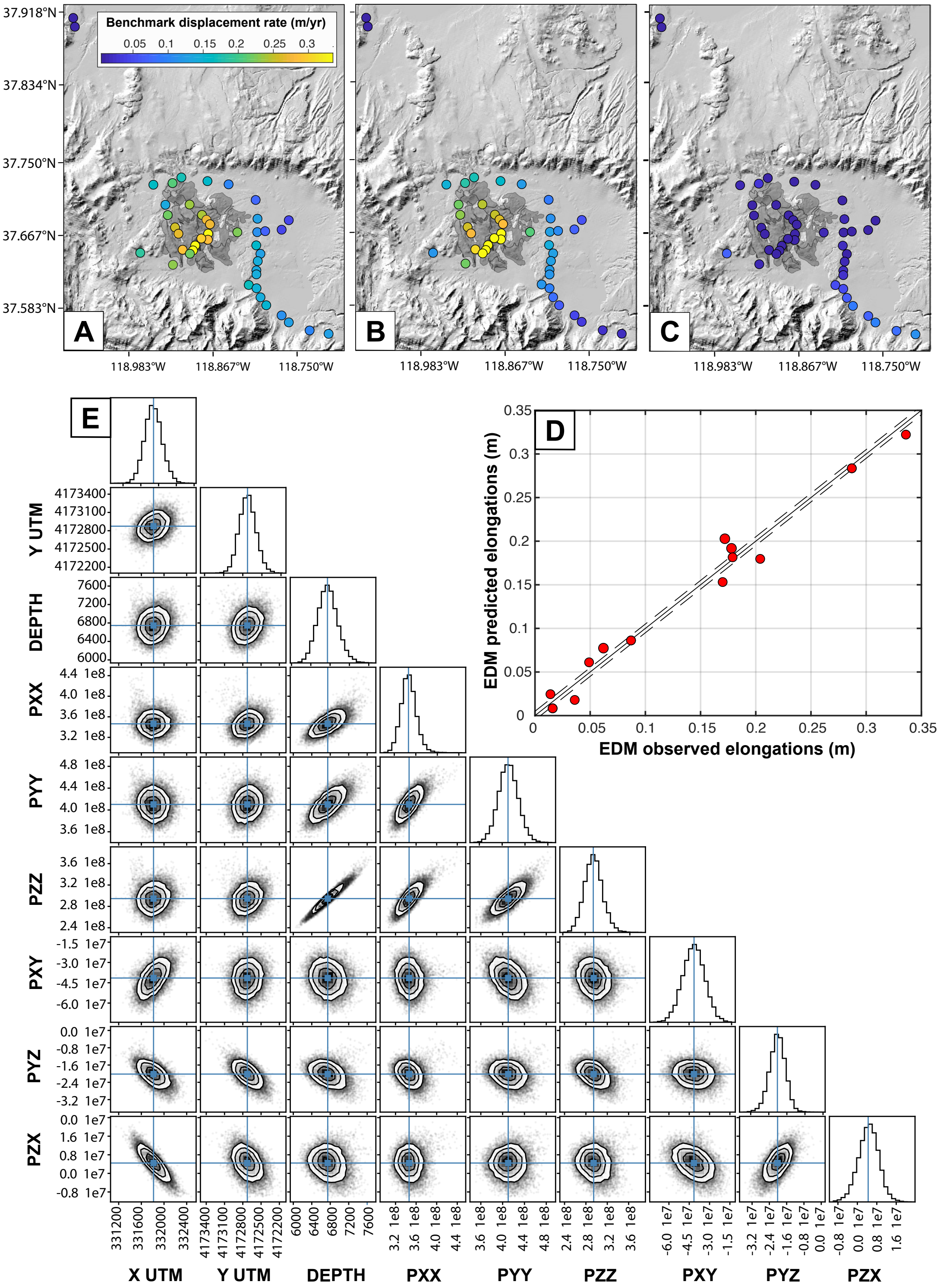

Figure S5. Model fit and parameters distributions for the unrest 85-99. a,b,c) Data, Model, Residual of Leveling data. d) correlation of observed and predicted EDM data. e) Parameters distributions (PPD) and mean values.